

DONOR-ACCEPTOR TYPE BULK NANO-HETEROJUNCTION SOLAR CELL  
DESIGNS BASED ON ELECTRONICALLY COUPLED LEAD SELENIDE  
NANORODS AND LEAD SELENIDE QUANTUM DOTS

A THESIS SUBMITTED TO  
THE GRADUATE SCHOOL OF NATURAL AND APPLIED SCIENCES  
OF  
MIDDLE EAST TECHNICAL UNIVERSITY

BY

İREM KOLAY

IN PARTIAL FULFILLMENT OF THE REQUIREMENTS  
FOR  
THE DEGREE OF MASTER OF SCIENCE  
IN  
CHEMISTRY

JULY 2022



Approval of the thesis:

**DONOR-ACCEPTOR TYPE BULK NANO-HETEROJUNCTION SOLAR  
CELL DESIGNS BASED ON ELECTRONICALLY COUPLED LEAD  
SELENIDE NANORODS AND LEAD SELENIDE QUANTUM DOTS**

submitted by **İREM KOLAY** in partial fulfillment of the requirements for the degree  
of **Master of Science in Chemistry, Middle East Technical University** by,

Prof. Dr. Halil Kalıpçılar  
Dean, Graduate School of **Natural and Applied Sciences**

Prof. Dr. Özdemir Doğan  
Head of the Department, **Chemistry**

Assist. Prof. Dr. Demet Asil Alptekin  
Supervisor, **Chemistry, Middle East Technical University**

**Examining Committee Members:**

Prof. Dr. Ali Çırpan  
Chemistry, Middle East Technical University

Assist. Prof. Dr. Demet Asil Alptekin  
Chemistry, Middle East Technical University

Prof. Dr. Seha Tirkeş  
Chemical Engineering, Atılım University

Assoc. Prof. Dr. Merve İçli Özkut  
Chemistry, Ankara University

Assist. Prof. Dr. Erol Yıldırım  
Chemistry, Middle East Technical University

Date: 22.07.2022

**I hereby declare that all information in this document has been obtained and presented in accordance with academic rules and ethical conduct. I also declare that, as required by these rules and conduct, I have fully cited and referenced all material and results that are not original to this work.**

Name Last name: İREM KOLAY

Signature:

## ABSTRACT

### **DONOR-ACCEPTOR TYPE BULK NANO-HETEROJUNCTION SOLAR CELL DESIGNS BASED ON ELECTRONICALLY COUPLED LEAD SELENIDE NANORODS AND LEAD SELENIDE QUANTUM DOTS**

Kolay, İrem  
Master of Science, Chemistry  
Supervisor: Assist. Prof. Dr. Demet Asil Alptekin

July 2022, 82 pages

Multiple exciton generation (MEG) process has received a great deal of attention in solar energy research due to its high potential in improving photocurrent. In this respect, PbSe NRs are considered as one of the most promising candidates due to their remarkable MEG yield. However, limited number of solar cell studies based on PbSe NRs and their poor performances have been limiting their utilization in photovoltaic (PV) technologies. In this thesis, previously introduced solar cell design, where covalently bonded PbSe QDs and PbSe NRs in a BNHJ layer were utilized as light absorbing layer, were further optimized and the direct roles of solar cell components and processing conditions are disclosed for the first time in literature. High quality QDs and NRs with low polydispersity were synthesized with hot injection method and characterized by techniques such as UV-Vis spectroscopy, TEM and UPS. Solar cells with inverted architecture were fabricated and characterized by I-V and EQE techniques. Performance of the solar cells was enhanced by optimizing the cell components such as light absorbing active layer, electron transport and hole transport layers. Optimization of the thicknesses of the active and electron transport layers, and heat treatment were found to be the key factors for improving the performance of the solar cells in terms of PCE and

EQE/IQE values at energies where the MEG is expected to take place. Additionally, we found that the type of the HTL has a profound affect in cell performance. In this sense, PbSe QDs with 1.4 eV band gap, PbS QDs with 1.3 eV band gap and TIPS-Pentacene molecule were utilized as HTLs. We found that PbSe QDs with 1.4 eV band gap leads to the best performing cells. Furthermore, we found that the structure of the ligand that holds NRs and QDs together in BNHJ layer has a drastic affect in cell performance. The optimized BNHJ devices lead to the best performing cells comprising PbSe NRs in literature; >100% EQE/IQE and 4.09% PCE.

Keywords: Quantum Dot, Nanorod, Multiple Exciton Generation, Bulk Nano - Heterojunction Solar Cells

## ÖZ

# ELEKTRİKSEL BAĞLAŞIM İÇİNDE OLAN KURŞUN SELENYUM NANO ÇUBUK VE KURŞUN SELENYUM KUANTUM NOKTA TEMELLİ ELEKTRON VERİCİ-ALICI TİPİ HETEROEKLEM GÜNEŞ HÜCRELERİNİN TASARIMI

Kolay, İrem  
Yüksek Lisans, Kimya  
Tez Yöneticisi: Dr. Öğr. Üyesi Demet Asil Alptekin

Temmuz 2022, 82 sayfa

Fotoakımı iyileştirmedeki yüksek potansiyeli nedeniyle çoklu eksiton oluşturma işlemi (MEG), güneş enerjisi araştırmalarında büyük ilgi görmektedir. Bu bağlamda, yüksek MEG verimine sahip PbSe nano-çubukları (NÇ) umut vadeden adaylardan biri olarak değerlendirilmektedir. Ancak, PbSe NÇ temelli, düşük performans gösteren sınırlı sayıda güneş pili çalışmasının rapor edilmesi, PbSe NÇlerinin fotovoltaiik teknolojilerinde kullanımlarını sınırlandırmaktadır. Bu tezde, kovalent bağlı PbSe KNler ve PbSe NÇlerin ışık soğurucu katman olarak kullanıldığı nano-heteroeklem güneş hücreleri optimize edilmiş ve literatürde ilk kez, hücre katmanlarının ve hücre üretim parametrelerinin tasarımıdaki rolleri araştırılmıştır. Düşük parçacık-boyut dağılımına sahip, yüksek kalitede KN ve NÇler sıcak enjeksiyon yöntemi ile sentezlenmiş ve Uv-Vis Spektrofotometre, TEM ve UPS teknikleri ile karakterize edilmiştir. Ters mimariye sahip güneş hücreleri üretilmiş, I-V ve EQE teknikleri ile karakterize edilmiştir. Güneş hücrelerinin performansları, aktif katman, elektron taşıma ve delik taşıma katmanlarının optimize edilmesiyle artırılmıştır. Aktif ve elektron taşıma katmanlarının kalınlık optimizasyonları ve ısıtım işlem uygulamalarının hücre verimini artırmada ve MEG beklenen dalga boylarında

EQE/IQE deęerlerini artırmada kilit role sahip oldukları tespit edilmiştir. Ek olarak, HTL tipinin hücre performansı üzerinde etkisi olduğu anlaşılmıştır. Bu bağlamda, HTL olarak 1.4 eV bant aralığına sahip PbSe KNler, 1.3 eV bant aralığına sahip PbS KNler ve TIPS-Pentacene molekülü kullanılmıştır. 1.4 eV bant aralığına sahip PbSe KNlerin HTL olarak kullanıldığı hücrelerin yüksek performansa sahip oldukları görülmüştür. Ek olarak, heteroeklem tabakayı oluşturan NÇ ve KNleri bir arada tutan ligand yapısının, hücre performansını önemli ölçüde etkilediği tespit edilmiştir. Gerçekleştirilen çalışmalar sonunda NÇ-KN temelli nano-heteroeklem güneş hücreleri bilinen en yüksek verime ulaşmıştır; >%100 EQE/IQE ve %4,09 PCE.

Anahtar Kelimeler: Kuantum Nokta, Nanoçubuk, Çoklu Eksiton Üretimi, Yığın Nano-Heteroeklem Güneş Pilleri,

To my beloved family...

## ACKNOWLEDGMENTS

First and foremost, I would like to express my sincere gratitude to my supervisor Assist. Prof. Dr. Demet Asil Alptekin for her guidance, advice, and encouragement throughout my graduate journey. Through these years, I have learned a lot from her both technically and personally. I am grateful for her excellent patience, guidance, and support. It is always my pleasure working with her.

This thesis would not be possible without our good friends and colleagues. First, I would like to thank all past and present Demet Asil Alptekin research laboratory members Batuhan Uzun and Dilara Naz Günaydın for being always kind, helpful and friendly to me. Specially, I would like to thank Firdevs Aydın who always be my side through this journey and responded whenever I asked for help.

I would like to thank to Prof. Dr. Atilla Cihaner from Atılım University for giving us to opportunity to use his solar cell fabrication facilities at ATOMSEL. Also, Thanks to Assoc. Prof. Dr. Emrullah Görkem Günbaş to allows me to use his laboratory for the thermal evaporator system. And I also thank to GÜNAM for the opportunity to use solar cell characterization set-up. In addition, I thank to METU Central Laboratory staff for TEM and UPS measurements. I am also grateful to Research Fund of the Middle East Technical University (Project Number: TEZ-YL-103- 2022-10860) for the financial support.

I would like to thank to my close friends especially my wingman Ali Ozan Karabüber, Duygu Cındız Harçcı, Mehmet Burak Uzun, Süheyla Yılmaz, Gökçe Tidim, Umut Aydemir, Doğan Akbulut, Gonca Ünder, my powerpuff girls Ceylin Ökten, Mine Gülnur Küçükıılmaz and Işıl Adadıođlu for their presence and support without them my life would be less colorful. I also thank to Deniz Yılmaz for being best shotgun! Also, I would like to thank to Şafak Tekir, Ođuzhan Karakurt, Osman Karaman and Furkan Melih Günay.

Finally, I would like to express my special thanks to my lovely family, my parents Kemal Kolay and Nevin Kolay and my brother Enes Kolay for being always there whenever I need them along with their endless support, patience, and confidence helped me throughout all my life. Without their unconditionally love and support, none of my success would be possible. I am thankful to have them.

## TABLE OF CONTENTS

ABSTRACT .....	v
ÖZ .....	vii
ACKNOWLEDGMENTS .....	x
TABLE OF CONTENTS .....	xii
LIST OF TABLES .....	xv
LIST OF FIGURES .....	xvi
LIST OF ABBREVIATIONS .....	xix
CHAPTERS	
1 INTRODUCTION .....	1
2 BACKGROUND .....	3
2.1 Quantum Dots & Nanorods .....	3
2.1.1 Synthesis of Quantum Dots and Nanorods.....	6
2.2 Solar Cells.....	10
2.2.1 PbSe QD and PbSe NR based solar cells working under MEG principle.....	18
3 EXPERIMENTAL .....	25
3.1 Materials .....	25
3.2 Synthesis .....	25
3.2.1 Lead Selenide Quantum Dot Synthesis .....	26
3.2.2 Lead Selenide Nanorod Synthesis .....	28
3.2.3 Lead Sulfide Quantum Dot Synthesis .....	29
3.2.4 Zinc Oxide Nanoparticle Synthesis .....	30

3.3	Material Characterization / Instrumentation.....	31
3.3.1	Absorption Spectroscopy .....	31
3.3.2	Transmission Electron Microscopy (TEM) .....	31
3.3.3	UV Photoelectron Spectroscopy (UPS).....	31
3.4	Solar Cell Fabrication.....	32
3.5	Solar Cell Characterization .....	36
3.5.1	Current-Voltage Measurement.....	36
3.5.2	Quantum Efficiency Measurement .....	36
4	RESULTS AND DISCUSSION .....	39
4.1	Characterization of PbSe QDs/NRs/SynPNRs and PbS QDs .....	39
4.2	Solar Cell Application .....	47
4.2.1	Effect of the Front QD Layer .....	48
4.2.2	Effect of Annealing of the BNHJ Active Layer.....	50
4.2.3	Optimization of the ZnO ETL.....	51
4.2.4	Effect of Active Layer Thickness on Cell Performance .....	56
4.2.5	Optimization of the HTL .....	59
4.2.6	Effect of Ligand Structure.....	63
5	CONCLUSION.....	67
	REFERENCES .....	69
	APPENDICES	
A.	APP-1 .....	79
	UPS spectrum of PbSe NR .....	79
B.	APP-2 .....	80
	UPS spectrum of SynP-PbSe QD .....	80

C.	APP-3.....	81
	UPS spectrum of PbSe QD.....	81
D.	APP-4.....	82
	UPS spectrum of TIPS-Pentacene.....	82

## LIST OF TABLES

### TABLES

Table 2.1 Summary of the solar cell studies based on PbSe QDs and NRs with highest efficiency.....	22
Table 3.1 Synthesis parameters for QDs with different band gaps.....	28
Table 3.2 Spin coating parameters and the characteristics of the NP solutions.....	34
Table 4.1 Band gap and size properties (average diameter (D) and average length (L)) of PbSe QDs and NRs used in solar cell studies. ....	44
Table 4.2 Band edge energies of the EDT capped PbSe QDs, PbSe NRs, PbS QDs and TIPS-Pentacene with respect to vacuum. ....	46
Table 4.3 Effect of PbSe QD <sub>1.0 eV</sub> front layer on solar cell characteristics. ....	49
Table 4.4 Effect of annealing of the light absorbing active layer on the cell performance. ....	51
Table 4.5 Effect of annealing duration of ZnO on solar cell characteristics. ....	53
Table 4.6 Effect of annealing temperature and dilution ratio of ZnO on solar cell characteristics.....	56
Table 4.7 Effect of active layer thickness on cell performance parameters. ....	59
Table 4.8 Effect of the HTL on the cell performance parameters. ....	62
Table 4.9 Effect of ligand structure on the cell performance parameters.....	66

## LIST OF FIGURES

### FIGURES

Figure 2.1. Schematic representation of the relation between the size of the nanocrystal and bandgap energy ( $E_g$ ). Bandgap energy of <b>a</b> ) a bulk semiconductor, <b>b</b> ) NCs of varying particles sizes, and <b>c</b> ) atoms. The emission energy of the NC, under quantum confinement affect, increases as the size decreases.....	4
Figure 2.2. <b>a</b> ) Schematic representation of a typical set up utilized in hot injection method. <b>b</b> ) Schematic representation of the nucleation and growth mechanisms based on the LaMer-Dinegar model. <b>c</b> ) Absorbance spectra of QDs with different size distribution. ....	7
Figure 2.3. AM1.5 spectrum solar energy distribution in the earth's atmosphere <sup>35</sup> . Distribution ratios for the UV, Vis and infrared regions are indicated as 6.6%, 44.7% and 48.7%, respectively. ....	11
Figure 2.4. Current-Voltage characteristics of a solar cell <sup>36</sup> . ....	12
Figure 2.5. Chart of the best efficiencies for several research solar cells <sup>41</sup> .....	16
Figure 2.6. <b>a</b> ) Schematic representation of MEG process <sup>48</sup> Step 1: Incident photon absorption; electron excitation leaves a hole behind. Step 2: Relaxation of the excited electron. Step 3: Excitation of another electron from the valence band to the conduction band. <b>b</b> ) Spectroscopic study that shows how the quantum efficiency changes with the band gap of PbSe NRs (green), PbSe QDs (blue) and bulk PbSe <sup>49</sup> . ....	19
Figure 3.1. Schlenk line for the synthesis of air sensitive PbSe QDs and NRs.....	27
Figure 3.2. Nitrogen filled glove box to create an oxygen free environment for the processing of oxygen-sensitive materials.....	28
Figure 3.3. UPS spectrum of 0.95 eV PbSe NR.....	32
Figure 3.4. Schematic representation of solar cell fabrication process. ....	33
Figure 3.5. Schematic representation of L-B-L spin coating process. ....	35

Figure 3.6. External/internal quantum efficiency measurement setup and calibration standards. <b>a)</b> Newport QUANTX-300 apparatus. <b>b)</b> Ongoing measurement on a solar cell attached to a test holder. <b>c)</b> Silicon test cell. <b>d)</b> Calibrated silicon-germanium reference detector. <b>e)</b> High and Low calibrated reflectance standards for the IQE tests. ....	38
Figure 4.1. Absorbance spectra of the QDs and NRs in octane and thin film <b>a)</b> PbSe NRs (0.95 eV), <b>b)</b> PbSe QDs (1.0 eV), <b>c)</b> PbSe QDs (1.4 eV), <b>d)</b> PbSe QDs (1.85 eV) and <b>e)</b> PbS QDs (1.3 eV).....	40
Figure 4.2. Absorbance spectra of the three different blends. <b>a)</b> Bulk-1: PbSe QDs (1.0 eV) + PbSe NRs (0.95 eV). <b>b)</b> Bulk-2: PbSe QDs (1.4 eV) + PbSe NRs (0.95 eV). <b>c)</b> Bulk-3: PbSe QDs (1.85 eV) +PbSe NRs (0.95 eV). ....	41
Figure 4.3. TEM images of <b>a)</b> EDT capped PbSe NRs with band gap 0.95 eV (scale bar: 50 nm), <b>b)</b> EDT capped PbSe QDs with band gap 1.0 eV (scale bar: 20 nm), <b>c)</b> Bulk-1: PbSe NRs with 0.95 eV with 1.0 eV QDs (scale bar: 50 nm). <b>d)</b> Bulk-2: PbSe NRs with 0.95 eV with 1.4 eV QDs (scale bar: 50 nm), <b>e)</b> Bulk-3: PbSe NRs with 0.95 eV with 1.85 eV QDs (scale bar: 50 nm).....	43
Figure 4.4. UPS measurements of EDT capped <b>a)</b> PbSe QDs (1.0 eV), <b>b)</b> PbSe NRs (0.95 eV), <b>c)</b> PbSe SynP-NRs (0.88 eV) and <b>d)</b> TIPS-Pentacene. ....	45
Figure 4.5. UPS measurements of Bulk-1, where the NPs are EDT capped. ....	46
Figure 4.6. Role of PbSe QD <sub>1.0 eV</sub> front layer on the photovoltaic performance of the solar cell. <b>a)</b> Schematic representation of cell architectures. <b>b)</b> I-V characteristics and, <b>c)</b> EQE/IQE spectra. ....	48
Figure 4.7. Role of annealing of light absorbing layer on the photovoltaic performance of the solar cell. <b>a)</b> I-V characteristics and, <b>b)</b> EQE/IQE spectra.....	50
Figure 4.8. Role of the annealing duration of the ZnO layer on the photovoltaic performance of the solar cell. <b>a)</b> Cell architecture, <b>b)</b> I-V characteristics and <b>c)</b> EQE/IQE spectra.....	53
Figure 4.9. Role of the dilution ratio and the annealing temperature of the ZnO layer on the photovoltaic performance of the solar cell. <b>a)</b> Cell architecture, <b>b)</b>	

transmittance spectrum of ZnO thin films, <b>c)</b> I-V characteristics and <b>d)</b> EQE/IQE spectra.....	55
Figure 4.10. Role of the active layer thickness on the photovoltaic performance of the solar cell. <b>a)</b> Schematic representation of cell architectures, <b>b)</b> I-V characteristics and <b>c)</b> EQE/IQE spectra. ....	57
Figure 4.11. Role of the HTL on the photovoltaic performance of the solar cell. <b>a)</b> Schematic representation of the cell architecture, <b>b)</b> absorbance spectra of EDT capped light absorbing active layer (Bulk-1) and its components; EDT capped SynP-PbSe NR <sub>0.95 eV</sub> and EDT capped PbSe QD <sub>1.0 eV</sub> , <b>c)</b> energy landscape of cell components determined from UPS, <b>d)</b> absorbance spectra of TIPS-Pentacene, EDT capped PbSe QD <sub>1.4 eV</sub> and EDT capped PbS QD <sub>1.3 eV</sub> as HTLs, <b>e)</b> I-V characteristics and <b>f)</b> EQE/IQE spectra.....	61
Figure 4.12. Role of the ligand structure on the photovoltaic performance of the solar cell. <b>a)</b> Cell architecture and energy landscape of the cell components, <b>b)</b> TEM image of and BDT exchanged NRs thin film, <b>c)</b> TEM images of EDT exchanged NRs thin film, <b>d)</b> I-V characteristics and <b>e)</b> EQE/IQE spectra. ....	64
Figure 6.1. UPS spectrum of PbSe NR.....	79
Figure 6.2. UPS spectrum of SynP-PbSe NR.....	80
Figure 6.3. UPS spectrum of PbSe QD .....	81
Figure 6.4. UPS spectrum of TIPS-Pentacene.....	82

## LIST OF ABBREVIATIONS

### ABBREVIATIONS

ACN: Acetonitrile

BDT :1,3-Benzenedithiol

BNHJ: Bulk Nano-heterojunction

BP: Boiling Point

CdSe: Cadmium Selenide

CdTe: Cadmium Telluride

DEZn: Diethylzinc

DPP: Diphenyl Phosphine

EDT: 1,2-Ethanedithiol

E<sub>g</sub>: Band gap

ETL: Electron Transport Layer

EQE: External Quantum Efficiency

GB: Glove Box

FF: Fill Factor

HTL: Hole Transport Layer

I<sub>MP</sub>: Current at the Maximum Power Point

I<sub>sc</sub>: Short Circuit Current

IPA: Isopropyl Alcohol

ITO: Indium Tin Oxide

IQE: Internal Quantum Efficiency

I-V: Current-Voltage

J<sub>sc</sub>: Short Circuit Current Density

LED: Light Emitting Diode

LBL: Layer by Layer

MEG: Multiple Exciton Generation

MeOH: Methanol

MoO<sub>x</sub>: Molybdenum Oxide

NCs: Nanocrystals

NIR: Near-infrared

NPs: Nanoparticles

NRs: Nanorods

NREL: National Renewable Energy Center

NWs: Nanowires

OA: Oleic Acid

ODE: Octadecene

PbO: Lead (II) Oxide

PbS: Lead Sulfide

PbSe: Lead Selenide

PbTe: Lead Telluride

PCE: Power Conversion Efficiency

P<sub>MP</sub>: Maximum Power Point

PV: Photovoltaic

QDs: Quantum Dots

SynP: Growth Phase Surface Passivation Method

TCE: Tetrachloroethylene

TDP: Tris(diethylamino)phosphine

TDPA: Tetradecyl Phosphonic Acid

TEM: Transmission Electron Microscopy

THF: Tetrahydrofuran

TIPS-Pentacene: 6,13-bis(triisopropylsilylethynyl)pentacene

UPS: Ultra-Violet Photoelectron Spectroscopy

UV: Ultra-Violet

Vis: Visible

$V_{MP}$ : Voltage at The Maximum Power Point

$V_{OC}$ : Open Circuit Voltage

TCE: Trichloroethylene

TOP: Trioctylphosphine

ZnO: Zinc Oxide



## CHAPTER 1

### INTRODUCTION

Nanotechnology and nanoscience owe their inception to Richard Feynman's talk at the California Institute of Technology on December 29, 1959. Feynman's explanation about how atoms or molecules can be arranged, controlled, and manipulated by a scientist has ensured that nanotechnology and nanoscience applications have been at the forefront of research studies for years.

Optoelectronic advancements also enable plentiful cooperation for nanostructured materials in this field. Improved and unique optoelectronics areas, such as energy harvesting and photodetectors, have become widespread and popular issues in nanotechnology field. As the silicon technology approaches the theoretical limits (33 % photo conversion efficiency (PCE), crystalline silicon solar cell's highest achievable PCE under one sun illumination<sup>1</sup>), third generation solar cells are being developed in an effort to harness solar energy in a more effective manner<sup>2,3</sup>. Third generation solar cells, for instance, are being created using nanoparticle (NP) that incorporate quantum dots (QDs), nanorods (NRs), or nanowires (NWs). The losses arising from non-absorbed infrared and ultraviolet regions of the sun spectrum are one of the fundamental reasons behind crystal silicon solar cells' 33 % theoretical limit (Shockley- Queisser limit)<sup>1</sup>. Lead chalcogenide NPs are advantageous and intriguing prospects for solar cell applications owing to their exceptional characteristics, such as high exciton Bohr radius, tunability of their band gap, MEG and near-infrared absorption. However, mid gap state in their band gap and insufficient knowledge about surface chemistry of lead chalcogenide NP prevent their widespread use in the solar energy sector.

In this thesis, a comprehensive approach targeting the charge extraction and transport has been investigated by forming donor-acceptor type bulk nano-heterojunction (BNHJ) solar cells based on PbSe nanorods and PbSe quantum dots.

In Chapter 2, background information that aids understanding and examination of the experimental investigation is provided. First, some background information on QDs and their optoelectronic features are offered. Synthesis methods for producing NPs, as well as the operation of solar cells, are covered. Chapter 2 continues with a summary of previous reports that inspire my thesis study and finalizes with the introduction of my motivation behind this thesis study.

In Chapter 3, all of the experimental methodologies utilized in this study are described. Detailed synthetic procedures of the NPs such as lead selenide (PbSe) QDs, PbSe NRs and lead sulfide (PbS) QDs are provided in the first part of Chapter 3. In the second part, sample preparation and characterization procedures are described. In the final part, quantum dot/rod based BNHJ solar cell fabrication and characterization protocols are introduced.

In Chapter 4, synthesized high quality QDs and NRs with high monodispersity were characterized by techniques such as uv-vis spectroscopy, transmission electron microscopy (TEM) and ultra-violet photoelectron spectroscopy (UPS) in the first part of Chapter 4. In the second part, effect of electron transport layer (ETL), hole transport layer (HTL), thickness of active layer, heat treatment of active layer and ligand structure were investigated for BNHJ solar cell.

In Chapter 5, conclusion for the characterization of PbSe QDs, PbSe NRs and PbS QDs and solar cell application studies for PbSe QDs and PbSe NRs are stated.

## CHAPTER 2

### BACKGROUND

#### 2.1 Quantum Dots & Nanorods

QDs, a type of zero-dimensional semiconductor nanocrystals (NCs), are one of the most accomplished nanoscale building blocks<sup>4</sup>. They have tiny size that makes possible to confine the movement of their charge carriers (electron - hole) inside all three dimensions within a nanometer-sized region. Through the synthesis, their unique chemical, physical and optoelectronic properties, especially shape, size, and size distribution are easily tunable. This makes quantum dots fascinating candidates for use in applications such as bioimaging, infrared photodetectors, lasers, light-emitting diodes, and solar cells<sup>2,5,6,7,8</sup>. The difference between the highest occupied energy level and lowest occupied energy levels, defined as the band gap of the material is directly regulated by the size and size distribution of the QDs<sup>9,10</sup>. The popularity of the QDs has grown rapidly in recent decades owing to their efficient separation and transportation of the charges, their quantum confinement phenomena and hot exciton (electron and hole pair) generation property<sup>10</sup>. Furthermore, bandgap tunability of the QDs proposes new possibilities for harvesting the light energy across the full solar spectrum. Near-infrared (NIR) active lead chalcogenide QDs, such as PbS, PbSe, and lead telluride (PbTe), with large Bohr radius (for PbS ~ 18 nm<sup>11</sup>, for PbSe ~ 46 nm<sup>12</sup> and for PbTe ~150 nm<sup>11</sup>), narrow band gaps, and the ability to generate multiple excitons (multiple excitons generation, MEG) have attracted interests from broad range of researchers in optoelectronics field<sup>10</sup>.

Even though QDs and their bulk semiconductor forms have the same composition, their optical properties differ from their bulk form due to their extremely small size which ranges from 1 to 10 nm<sup>13</sup>. Bulk semiconductors have a natural length scale, called as the exciton Bohr radius, for electronic excitations. This dictated by the

intensity of the Coulomb contact between electron and hole pair for electronic excitations and it is. However, this feature differs in ultra small semiconductor elements belonging to the IV, III-V, and II-VI groups. The spatial distance between the electron and hole pair is dictated by the dimensions of the NPs rather than the strength of Coulomb interaction between the electron and hole, if the size of the NPs is same or smaller than the Bohr radius. This is referred as quantum size effect. This effect is a phenomenon in which the electronic energies are directly proportional to the degree of spatial confinement of electronic wave functions and NP dimensions<sup>14,15</sup>. With the help of quantum size effect, the emission color and the spectral onset of the absorption can be controlled by changing the band gap of the NP.

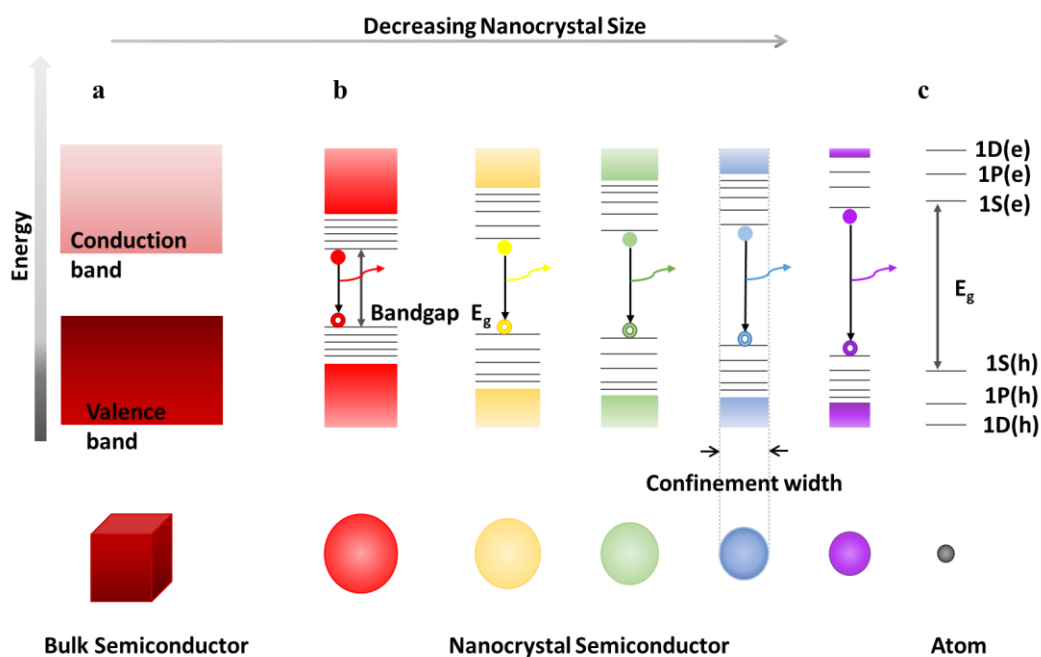


Figure 2.1. Schematic representation of the relation between the size of the nanocrystal and bandgap energy ( $E_g$ ). Bandgap energy of **a**) a bulk semiconductor, **b**) NCs of varying particles sizes, and **c**) atoms. The emission energy of the NC, under quantum confinement affect, increases as the size decreases.

As represented by the scheme in Figure 2.1, while going from bulk material to a small NC, structure of the energy levels changes; when size becomes lower than of the Bohr radius, charge carriers are confined in the QDs, and continuous energy bands of a bulk material are replaced by the discrete energy levels. Due to the resemblance of the discrete nature of the energy levels of QDs to the atomic orbitals', QDs are generally called as "artificial atoms"<sup>16</sup>.

As represented in Figure 2.1b, emission wavelength depends on the size of the NC; as the size of QDs increases, emission wavelength shifts to lower energy side. The relationship between the bandgap and size in Figure 2.1-b is expressed by the Brus equation in equation 1<sup>17</sup>. A basic particle-in-a-box potential model can be used to represent this effect<sup>15</sup>. This model predicts that the size-dependent contribution to the energy gap for a spherical QD with radius  $R$  is simply proportional to  $1/R^2$ . The Brus equation can explain this relation;

$$\Delta E(R) = E_G(R) + \frac{\hbar^2}{8R^2} \left( \frac{1}{m_e^*} + \frac{1}{m_h^*} \right) \quad \text{Eq. 1}$$

$\Delta E(R)$ : emission energy,

$E_G(R)$ : bandgap energy,

$\hbar$ : Planck's constant,

$R$ : QD's radius,

$m_e^*$ : excited electron's effective mass,

$m_h^*$ : excited hole's effective mass<sup>17</sup>

While QDs are isotropic (homogeneous and uniform) materials, NRs are type of anisotropic (inhomogeneous and nonuniform) materials and because of their unique structure-dependent capabilities, they have widespread use in solar energy

conversion, thermoelectric devices, and energy storage technologies<sup>18</sup>. NRs, a type of one-dimensional semiconductor nanocrystals, are also known as needle like materials since their one direction is out of nanometer scale range. NRs have more ability of enhance electrical field compared to the spherical particles owing to their higher aspect ratio, which leads to an increased stimulation of surface plasmons. The strength of the dipole moment within a nanoparticle is particularly strong due to the increase in the surface plasmons. As a result, as compared to spherical particles, an increase in the surface plasmons leads to an increase in the electrical field in nanorods<sup>18</sup>. Alivisatos and colleagues showed the benefits of a rod-like form by observing partly aligned cadmium selenide (CdSe) NRs which offered an effective, guided channel for charge carriers to pass across a photovoltaic device<sup>19</sup>. As the aspect ratio went from 1 to 10, adding nanorods to poly(3-hexylthiophene (P3HT) polymer film could increase the EQE 3 fold at 515 nm<sup>19</sup>.

### **2.1.1 Synthesis of Quantum Dots and Nanorods**

In order to get the required characteristics of NPs, it is necessary to select the most appropriate synthesis process and regulate the reaction conditions. Due to its low cost, straightforward preparation and high manufacturing yield, hot injection synthesis method is the most extensively utilized synthesis method for the PbX QDs (X: Se, S, Te). This method involves fast nucleation and continuous growth steps<sup>20</sup>. Crystals of varying sizes and forms can be produced by manipulating the conditions of the reaction, which include the reactivity and concentration of the precursors, the temperature at which the injection and growth processes take place, and the duration of the growth process<sup>21</sup>. The contemporary methods to produce monodisperse NPs are largely based on the LaMer and Dinegar's description. According to this explanation, the formation of monodisperse NPs needs a temporally distinct nucleation, proceeded by slower and regulated development on the nuclei that have already formed<sup>22,23</sup>. The colloidal synthesis system is made up of metal precursors, organic surfactants, and solvents according to the LaMer-Dinegar model of colloidal NP formation<sup>24</sup>.

A typical NP synthesis, as schematically shown in Figure 2.2-a, begins with an introduction of suitable molecular precursors into a reaction mixture to generate 'monomers' (I) for the uniform nucleation (II) of NPs and continues with further growth because of the constant flow of monomers onto the NP's surface (III). As shown in the Figure 2.2-b, depletion of the monomer concentration causes the Ostwald ripening process (also known as Lifshitz–Slyozov–Wagner growth), which involves the formation of larger dots by dissolving smaller ones<sup>25,26</sup>. This process may cause a red shift in the absorbance spectra due to the formation of larger dots (with lower band gap) and may affect the quality of NPs by deteriorating the size distribution. To avoid the Ostwald ripening process, growth time should be controlled.

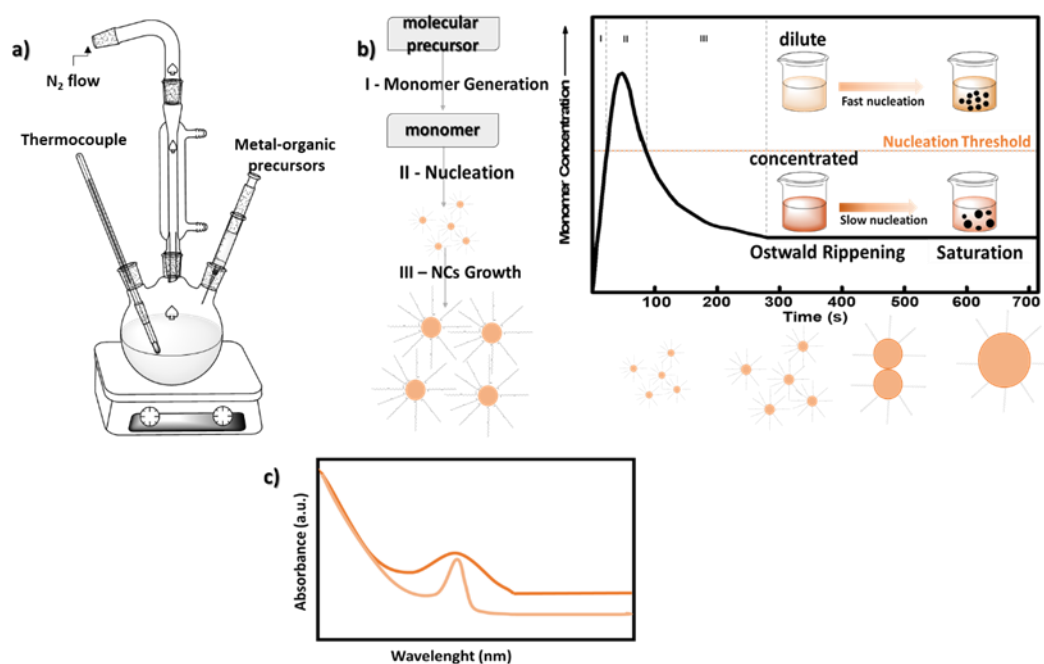
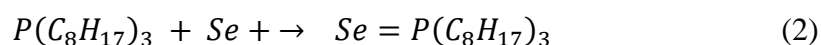
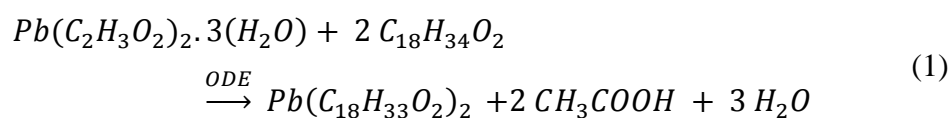
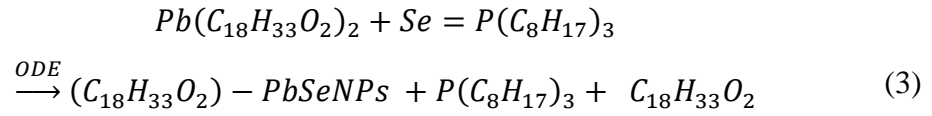


Figure 2.2. **a)** Schematic representation of a typical set up utilized in hot injection method. **b)** Schematic representation of the nucleation and growth mechanisms based on the LaMer-Dinegar model. **c)** Absorbance spectra of QDs with different size distribution.

The presence of surface capping molecules, often known as surfactants or stabilizers, can drastically modify all these subsequent steps. In the process of NP nucleation and growth, these capping molecules (ligands) such as alkylamines, alkyl phosphines, alkyl phosphine oxides, alkyl thiols, long chain carboxylic acids and phosphonic acids dynamically bind to the NP surfaces and provide the colloidal stability. Furthermore, the initial concentration of the stabilizers has a profound impact on NP quality and monodispersity<sup>27</sup>. As shown in Figure 2.2-b, higher concentration of capping ligands induces slow nucleation with a wide size distribution, whereas lower concentration causes fast nucleation with a uniform size distribution. After the concentration of monomers reaches a nucleation threshold, La Mer and Dinegar proposed a "burst" nucleation idea, which is associated with the fast nucleation<sup>4,23</sup>. Consequently, the approach in which one of the precursors is rapidly injected into another in a hot solvent to produce monomers with rapid nucleation is known as the hot injection method. To increase the reaction temperature range, non-coordinating, chemically inert liquids with high boiling points (BP) are preferred. In addition to the injection speed and concentration of the capping ligand, growth time, temperature of the injection, growth mechanism and concentration of the precursors also influence the size and size distribution of the NPs<sup>28</sup>.

The formation reactions of PbSe NPs are shown in the following reactions. Synthesis begins with the preparation of the lead precursor. Lead (II) acetate trihydrate (or lead (II) oxide, (PbO)) is coordinated at elevated temperature in a solvent with high BP to produce oleate capped lead (reaction 1). Se precursor is prepared by mixing n-trioctylphosphine (TOP) with selenium powder (reaction 2). As a product of following reaction (reaction 3), oleate capped PbSe NPs are obtained.





Nucleation and growth mechanism of the NPs take place in the solution phase containing organic capping ligands (surfactant molecules) that cling to the surface of the developing crystals. Oleic acid (OA) is a popular choice for capping agent which are utilized for the stabilization of the QDs and passivation of the dangling bonds on their surfaces. 1-octadecene (ODE) with a BP of 314.4°C is the most widely employed solvent in the synthesis process.

The type and stabilizing agent concentration control the shape and morphology of the NPs during synthesis. Selective adhesion of the capping ligands onto the NP surface leads to the formation of various crystal facets and the transformation of NP from almost spherical (0D) to highly anisotropic (1D, 2D and 3D) shapes, such as cubes, hollow rings, rods, or stars<sup>29</sup>. A comparison of the isotropic and anisotropic shaped inorganic NPs reveals the new physical and chemical features of the anisotropic shaped NPs with a high surface area to volume ratio<sup>30</sup>. Cubic, dodecahedral, octahedral, and tetrahedral NPs are included in 0D morphologies, whereas 1D forms include hollow NPs, nanoneedles, nanorods and nanowires. Belts, hollow rings, and sheets are classified as 2D, whereas nano flowers and nano stars belong to the 3D shape family<sup>29</sup>. The surfactant injection temperature, precipitation, additives, reaction medium pH and seeds are also effective mediators for the anisotropically driven morphology transition<sup>30</sup>. In this sense, tris(diethylamino)-phosphine (TDP) was used as coordinating solvent stabilizing agents to synthesize PbSe NRs<sup>31</sup>.

## 2.2 Solar Cells

QD applications are being utilized by an increasing number of businesses annually. Today, QDs are goods that are available for purchase on the market and are distributed in the form of dispersions. The primary application domains encompass a broad spectrum of optoelectronics, including detectors, lasers light emitting diodes (LEDs) and solar cells. This thesis concentrates on the solar cell applications of QDs and NRs.

The sun, a massive energy source that emits 95 % of its output energy as light, is an average star that has been burning for over four billion years<sup>32</sup>. Solar energy distribution in the earth's atmosphere is represented in Figure 2.3. Each of the invisible and visible radiations of the solar spectrum have different energies. Light in the ultraviolet (UV) region, that cannot be detect by human eye but may cause skin tanning, has more energy than the light in visible (VIS) region, that can be detect by the human eye. Light in the infrared (IR) region, that cannot be seen by the human eye but felt as heat by the skin, has the lowest energy across the solar spectrum.

Direct sunlight does not completely penetrate to the earth's atmosphere. The majority of the X-rays and significant amount of the UV radiation are attenuated by the atmosphere before reaching the ground. Some radiation is scattered randomly by the atmosphere, while some is reflected back from the ground into the space. In this sense air mass (AM) is a phrase that refers to the quantity of sunlight that reaches the surface of the earth and is related to the distance that light travels through the atmosphere and angle of radiation that is arriving to the surface. Air mass zero (AM0) refers to the region outside of the atmosphere in which there is no attenuation of solar radiation caused by the atmosphere. There are also other spectra, such as AM1 and AM1.5, which are designated for solar radiation under certain parameters, such as the angle at which the sunlight arrives or the inclination of the earth in relation to the sun<sup>33</sup>. When the sun at the zenith position, where the angle is equal zero, AM1 is used to refer the solar radiation at the earth surface. Figure 2.3 shows that AM1.5 (where the sun is at zenith angle 48.2°) spectra, which is a standard

calibration for the PV cells, based on a certain set of conditions and air mass<sup>34</sup>. Under standard pressure (1013.25 millibars) at sea level, total irradiance for the AM1.5 is  $100 \text{ mW/cm}^2$ <sup>35</sup>.

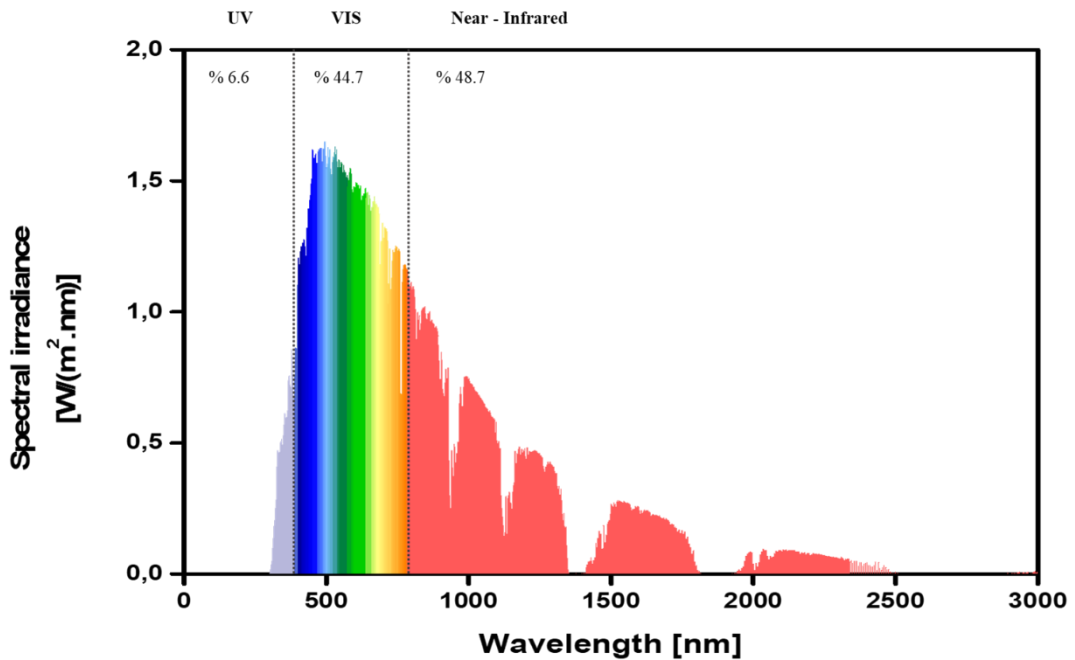


Figure 2.3. AM1.5 spectrum solar energy distribution in the earth's atmosphere<sup>35</sup>. Distribution ratios for the UV, Vis and infrared regions are indicated as 6.6%, 44.7% and 48.7%, respectively.

Solar cells are the most fundamental form of photovoltaics, which are devices that allow photons to remove electrons from an atom in order to generate energy. The efficiency of the cells is usually described in terms of  $\eta$  which is affected by several factors, including the type of material, layer design, preparation procedure, and incident radiation. Current-voltage (I-V) characteristics at a specified temperature and irradiance can be used to calculate a cell's efficiency. Open circuit voltage ( $V_{oc}$ ), short circuit current ( $I_{sc}$ ), fill factor (FF), PCE, shunt resistance ( $R_{SH}$ ), and series resistance ( $R_s$ ) are all determined from the I-V characteristics of the cells. All I-V characteristics parameters are represented in Figure 2.4.

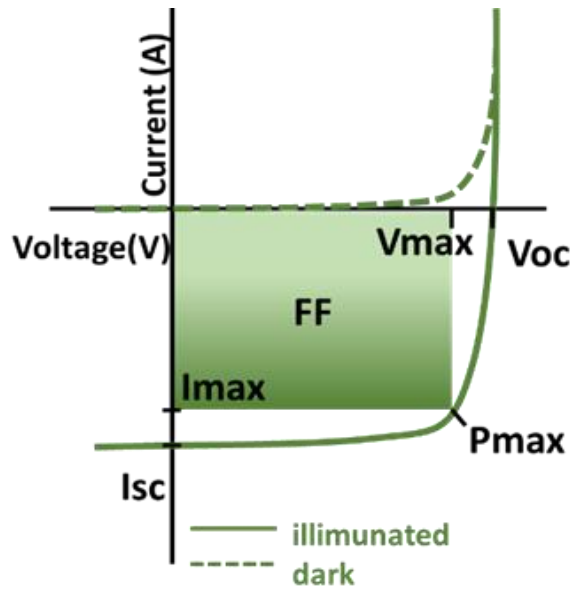


Figure 2.4. Current-Voltage characteristics of a solar cell<sup>36</sup>.

$I_{sc}$  is the maximum current that can flow through a cell without causing damage to its structure and it is measured when the electrodes are short circuited, and the voltage of the cell is zero.  $I_{sc}$  relates to the carriers that are generated and accumulated upon illumination. Therefore, it relies on the solar radiation incident and the area of lighting. Typically, it is expressed as short circuit density ( $J_{sc}$ ) by reducing area dependence.  $J_{sc}$  can be expressed as;

$$J_{sc} = \frac{I_{sc}}{A} \quad \text{Eq. 2}$$

where,  $A$  is the lighted area of the solar cell<sup>37</sup>.

$V_{oc}$  is the maximum voltage that is generated under illumination without current flow through a cell. The area of the solar cell and the incident light does not alter the open circuit voltage of an ideal solar cell in which photogenerated charges collected effectively without recombination. However, the device construction, photogenerated current and temperature affect  $V_{oc}$ <sup>34</sup>.  $V_{oc}$  can be expressed as;

$$V_{OC} = \frac{E_G}{q} - \eta k_B T \ln \frac{J_0}{J_L} \quad Eq. 3$$

$E_G$ : bandgap of the active material used in the solar cell,

$q$ : elementary charge,

$\eta$ : ideality factor,

$k_B$ : Boltzmann constant,

$T$ : solar cell's temperature,

$J_0$ : reverse saturation current,

$J_L$ : photocurrent<sup>38</sup>.

Assuming that the solar cell's net charge is zero, a rise in temperature has a lowering effect on the  $V_{oc}$ .

FF is defined as the ratio of the maximum power ( $P_{max}$ ) generated by the cell to the product of  $I_{sc}$  and  $V_{oc}$ . Maximum power ( $P_{max}$ ) is calculated from the product of maximum current ( $I_{max}$ ) and maximum voltage ( $V_{max}$ )<sup>38</sup>. FF can be expressed as;

$$FF = \frac{P_{max}}{I_{sc}V_{oc}} = \frac{I_{max}V_{max}}{I_{sc}V_{oc}} \quad Eq. 4$$

Efficiency ( $\eta$ ) is defined as the ratio of the maximum power ( $P_{max}$ ) to the power output of the incident radiation, which has an irradiation of 1000 W/m<sup>2</sup> and is defined by the AM1.5 spectrum. Efficiency can be expressed as;

$$\eta = \frac{P_{max}}{P_{in}} = \frac{I_{SC}V_{OC}FF}{P_{in}A} = \frac{J_{SC}V_{OC}FF}{P_{in}} \quad Eq.5$$

Apart from the I-V characteristics, EQE is another key parameter for the characterization of a solar cell. EQE is the ratio of the number of charge carriers extracted from a solar cell to the number of incident photons. EQE is expressed as a function of the wavelength (or energy) of incident light. EQE can be 100 % if all incident photons can be absorbed by the active components in the solar cell and all generated charge carriers can be collected from the solar cell's electrodes. Assume that 100 incident photons strike the solar cell, 20 of them are reflected from its surface, and then 60 charges are produced. This solar cell's EQE is calculated as 60% by definition. To account for the reflection and transmission losses occur outside the active layer, internal quantum efficiency (IQE) is also measured. IQE is a ratio of the number of charge carriers extracted from a solar cell to the number of absorbed incident photons from the solar cell. When the 20 of 100 incident photon are reflected from the surface of the solar cell, the actual number of photon that enter the solar cell is 80. Since this solar cell creates 60 charges from 80 photons, IQE of this solar cell is calculated as 75% (60/ (100-20)) by definition. The EQE measures how these optical losses affect a solar cell, while IQE measures how well photons that do not get reflected or sent out of the cell can make carriers that can be collected<sup>39</sup>.

When light or photons hit the active material and knock an electron loose, the electrons soak up the energy and jump to a higher energy level. Excitons are loose connections between excited electrons and the holes that remain in the ground state. Electricity is made when electrons and holes are taken out of the opposite electrodes. However, the amount of time that the electron stays in the excited state is so short that it may be hard to collect the charge carriers. Recombination is what happens when electrons meet a hole, and it is one of the main reasons why the PCE of a solar cell goes down.

Alexandre Edmund Becquerel was the first person to notice the photovoltaic effect in 1839. Around 1880, Charles Fritts built the first selenium-based PV cell with 1%

PCE<sup>40</sup>. Bell Laboratories scientists determined after 1953 that silicon is more efficient than selenium for use in practical PVs<sup>40</sup>. National Renewable Energy Laboratory (NREL) increased the conversion efficiency up to 30 % in 1994 using a gallium indium phosphide and gallium arsenide cell. Today, as the need for renewable energy increases, research and development studies are being carried out all over the world with the aim of producing efficient and affordable photovoltaics. In this sense, the best research cell efficiencies chart is represented in Figure 2.5.

# Best Research-Cell Efficiencies

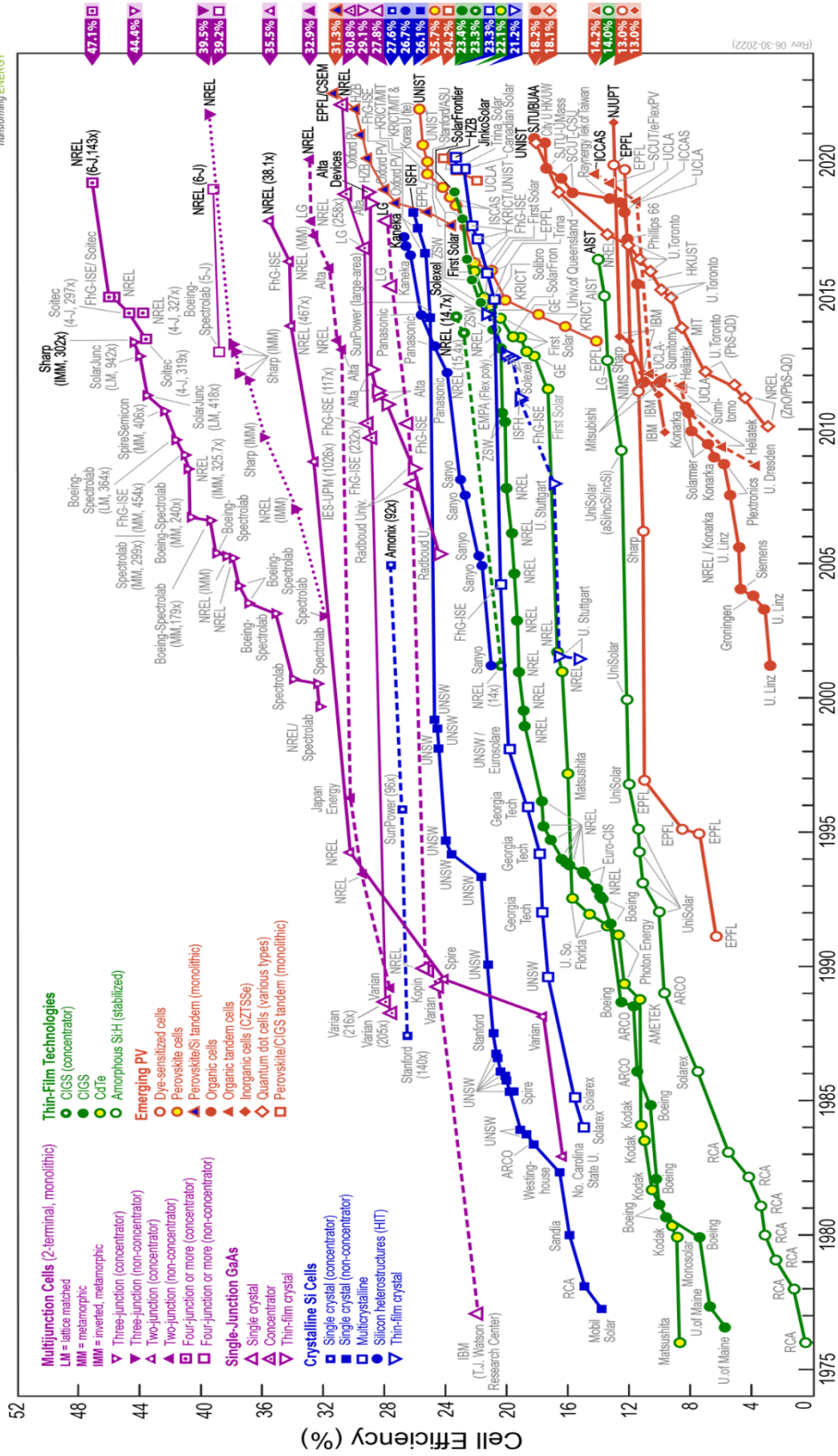


Figure 2.5. Chart of the best efficiencies for several research solar cells<sup>41</sup>.

Solar cells are classified as first, second or third generation cells<sup>42</sup>. First generation solar cells, which are also known as traditional, or wafer based solar cells, are durable and the most efficient solar cells includes monocrystalline silicon and polycrystalline silicon solar cells. Second generation solar cells, also known as thin film solar cells, are made of layers of semiconductor material that are only a few micrometers thick. Second generation solar cells such as cadmium telluride (CdTe), copper indium gallium diselenide (CIGD) and amorphous silicon solar cells are highly cost effective but have lower efficiency compared to the first generation solar cells. Third generation solar cells are more attractive than the first generation solar cells due to their lower manufacturing costs and improved efficiency by matching the solar radiation spectrum. Multijunction solar cells and upcoming PV technologies such as dye-sensitized solar cells (DSSCs), organic solar cells (OSCs), and quantum dot solar cells (QDSCs) are all part of the third generation of solar cells<sup>43</sup>. Inks, nanotubes, nanowires, nanoparticles, and conductive polymers are some examples of the brand-new materials that make up the solar cell category known as the third generation. Even the efficiencies of third generation solar cells are significantly lower than the other generation solar cells, the reduction in the fabrication costs and enhancement of the efficiency by making the absorption spectrum wider to match the spectrum of the solar radiation make third generation solar cells convenient and fascinating.

The amount of light that can be absorbed by a semiconductor is limited by its bandgaps. Semiconductors can absorb light if the material's bandgap is the same size or smaller than the photon's energy. According to Shockley-Queisser limit, which is a physical theory that describes the most efficient way that a photovoltaic can change light into electricity<sup>44</sup>. 33 % PCE is the maximum attainable efficiency for a single-junction solar cell with an optimal band gap of 1.34 eV. In addition, this limit indicates that the 67 % PCE loss mechanisms of solar cells where 47 % of loss is caused by turning light into heat, 18 % loss is caused by photons passing through the active material in the solar cell, and 2 % loss is caused by the recombination of charge carriers. According to recent studies, the process of MEG or hot carrier collection has a potential to exceed the theoretical Shockley–Queisser limit<sup>3,45–47</sup>. In this sense,

semiconductor materials that can generate multiple excitons from high energy photons, that were lost as heat for a generic semiconductor, have a great potential to exceed this limit.

### **2.2.1 PbSe QD and PbSe NR based solar cells working under MEG principle**

According to the theory behind traditional solar cells, each photon can only excite one electron through the bandgap of a semiconductor, and excess energy, photons with energies greater than that of the band gap of the semiconductor, is lost as heat. MEG, on the other hand, is a mechanism that enables the formation of more than one electron-hole pair in response to a single input photon. MEG can be seen in some semiconductors, such as PbTe, PbSe, and PbS QDs, and it has been widely researched in an effort to break the Shockley-Queisser limit<sup>46,28</sup>. MEG process occurs in three main steps as illustrated in Figure 2.6-a. Process starts with the absorption of an incident photon. An electron hole pair (exciton) is created in step 1 as represented in Figure 2.6.

During the second step of the process, the excited electron moves into the conduction band and releases some of its excess energy. When an additional electron on the valence band absorbs this surplus energy, which is either equal to or higher than the energy of the bandgap, the electron makes the transition into the conduction band, as seen in step 3. As a result, there is a potential to generate at least two electron-hole pairs upon single photon absorption, which corresponds to two times of the band gap of the semiconductor ( $2 \times E_G$ ).

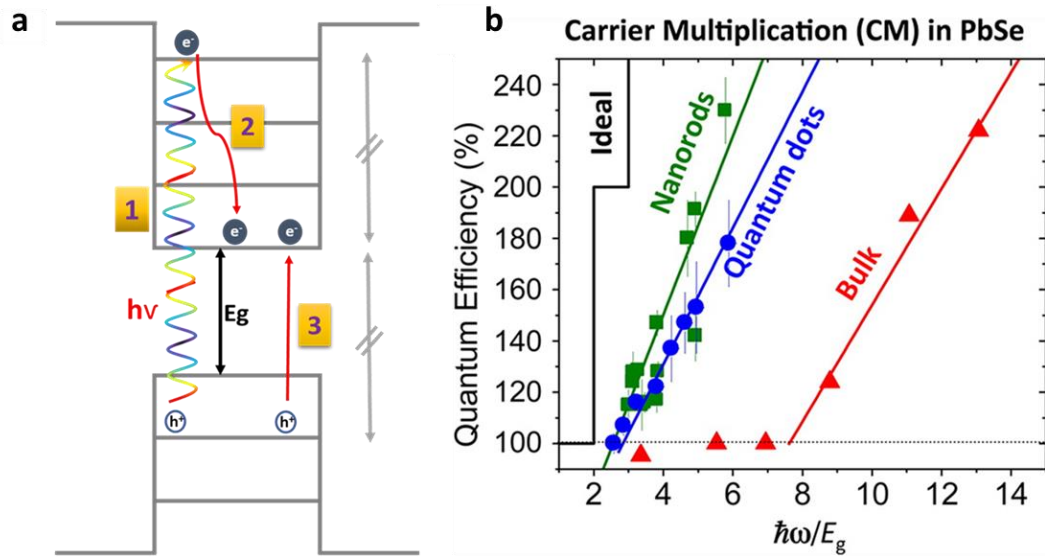


Figure 2.6. **a)** Schematic representation of MEG process<sup>48</sup> Step 1: Incident photon absorption; electron excitation leaves a hole behind. Step 2: Relaxation of the excited electron. Step 3: Excitation of another electron from the valence band to the conduction band. **b)** Spectroscopic study that shows how the quantum efficiency changes with the band gap of PbSe NRs (green), PbSe QDs (blue) and bulk PbSe<sup>49</sup>.

Theoretically, the MEG process takes place when the absorbed photons have an energy that is at least twice as great as the band gap ( $E_G$ ) of the NP. On the other hand, for bulk semiconductors, a greater activation energy is required for the excitation of numerous excitons. As can be seen in Figure 2.6-b, there is also a substantial relationship between MEG yield and the type of the material<sup>49</sup>. A recent study on lead-based semiconductors has shown that lead telluride (PbTe) QDs have the highest MEG yield, whereas PbS QDs have the lowest performance for the MEG process<sup>49</sup>. The yield of MEG can be affected not only by the composition but also by the form. According to Figure 2.6-b, for PbSe NRs to achieve a QE of 200 %, five times more energy than that of  $E_G$  is required. On the other hand, for PbSe QDs to achieve 200% QE, this number rises to six times that of  $E_G$ . Spectroscopic tests have shown that the quantum efficiency may be more than one hundred percent, which corresponds to the MEG process. However, difficulties associated with the extraction of the charge carriers prevent it from being used in the field of solar energy.

The use of QDs in photovoltaic solar cells is promising because they exhibit extremely high absorption coefficients as compared to their bulk equivalents. Another benefit of utilizing QDs in solar energy field is the wide range of absorption spectra that may be fine-tuned.

Schottky junction solar cells fabrication with lead chalcogenide QDs is straightforward. QDs are placed on indium tin oxide (ITO) substrates to produce an ohmic contact, and the Schottky junction is formed by the thermally evaporated metal electrodes<sup>50</sup>. Although the formation of Schottky junction solar cells is simple, their efficiencies are limited by three main factors: long distance that electrons travel through the film which leads to the recombination of electrons before reaching to the electrode collecting contact, low open circuit voltage ( $V_{oc}$ ) due to the defect states at the interface of the metal-semiconductor and hole injection barrier which leads to back recombination at the electron-extracting electrode<sup>51</sup>.

PbSe QD Schottky junction solar cell (ITO / PbSe QD / Ca / Al) showed a short circuit photocurrent of  $\sim 25 \text{ mA cm}^{-2}$  with a 2.1% PCE and yielded a peak EQE of 55 - 65 % below 800 nm<sup>52</sup>. Although PbSe QDs have high MEG efficiency, in this solar cell architecture, MEG was not observed.

The Schottky architecture's major drawbacks have lately been overcome by introduction of heterojunction solar cells. As of now, the highest-efficiency QD photovoltaic cells (14.00 % for PbS QDs, 10.68 % for PbSe QDs<sup>53</sup> and 2.52 % for PbSe NRs<sup>3</sup>) have been produced by combining two semiconductors with opposing doping types and bandgaps. There must be a type II heterojunction in order to efficiently dissociate photogenerated carriers: the electron acceptor must have a lower conduction band level while the electron donor must attract holes. Material requirements for a suitable band offset have been greatly reduced, and more materials are available for QD heterojunction solar cells<sup>51</sup>.

Although MEG is a key process to increase the solar cell efficiency by creating more than one electron with single absorbed photon, proof of concept on a working solar cell was achieved recently. Semonin et al. demonstrated the first PbSe QDs based

solar cell possessing MEG process<sup>47</sup>. In this study, PbSe QDs with 0.72 eV band gap was used and maximum EQE was measured as 106% 360 nm which corresponds to 2.8 times of QD band gap. Solar cell showed a high short circuit density approaching  $\sim 25 \text{ mA cm}^{-2}$  and a very low open circuit voltage of approximately  $\sim 0.1 \text{ V}$ . Another study demonstrated the MEG process for the first time for a solar cell based on PbSe NRs with 0.80 eV band gap<sup>3</sup>. They reported 122% EQE at 375nm which correspond to 4.2 times of the band gap of NRs. Despite the fact that remarkable EQE values have been published for PbSe NRs, the TEM pictures revealed non-uniform samples comprised of highly branched nanoparticles of varying shapes and sizes<sup>3</sup>. This makes difficult to assess the direct role of PbSe NRs in solar cell designs. Another study reported by Han et al. demonstrated the first PbSe NRs based solar cell which showed quite low short circuit current density  $0.062 \text{ mA cm}^{-2}$  and 0.003 PCE. Low current densities and PCE have been attributed to the pinholes formation and low NR packing density during spin coating process<sup>54</sup>.

Recently, Hacıfendioglu et al. suggested a bulk nano-heterojunction (BNHJ) platform in which the PbSe QDs are blended with PbSe NRs to create a donor-acceptor interface and prevent pinhole formation<sup>48</sup>. In this study, two cells made up of NRs only and a BNHJ layer are compared in order to examine the impact of the bulk nano-heterojunction concept. The BNHJ platform offered an improvement in  $J_{sc}$  (up to  $23 \text{ mA cm}^{-2}$ ) and  $V_{oc}$  (up to  $0.4 \text{ V}$ ). The higher PCE and FF of the cell 4.09 % and 42.99 % respectively comprising BNHJ layer were attributed to the improved film formation and effective photogenerated charge conduction between PbSe NRs and PbSe QDs.

Recent studies based on PbSe QDs and NRs with highest PCE and/or EQE are summarized in Table 2.1. According to Table 2.1, highest PCE has been reached when PbS QDs were used as HTL for PbSe QDs based solar cells which showed PbS QDs are a good candidate for PbSe QDs based solar cells as hole transport material. On the other hand, only PbSe QDs based solar cells showed lower MEG yield than PbSe NRs based solar cells.

Table 2.1 Summary of the solar cell studies based on PbSe QDs and NRs with highest PCE.

<b>Architecture</b>	<b>PCE %</b>	<b>Max EQE/IQE</b>	<b>Reference year</b>
ITO/ZnO/PbI <sub>2</sub> -capped PbSe QD (Eg :1.38 eV)/ PbS (Eg: 1.4 eV)-EDT/Au	10.68	-	Ahmad et al., 2019
ITO/ZnO/ PbSe QD (Eg :0.72 eV)-EDT+ Hy/Au	2.15	106 @ 360 nm (2.8xEg of QDs)	Semonin et al., 2010
ITO/ZnO/ PbSe QD (Eg :0.98 eV)-EDT+ Hy/Au	4.50	-	Semonin et al., 2010
ITO/ PEDOT:PPS/ PbSe NR (Eg :1.09 eV)-BDT/LiF/Al	0.03	-	Han et al., 2014
ITO/ZnO/ PbSe NR (Eg :0.80 eV)-EDT+ Hy/MoOx/Au	0.54	122 @ 375 nm (4.1xEg of QDs)	Davis et al., 2015
ITO/ZnO/ PbSe NR (Eg :0.95 eV)-EDT+ Hy/MoOx/Au	1.64	113 @ 375 nm (3.5xEg of QDs)	Davis et al., 2015
ITO/ZnO/ PbSe NR (Eg :1.05 eV)-EDT+ Hy/MoOx/Au	2.52	109 @ 375 nm (3.14xEg of QDs)	Davis et al., 2015
ITO/TiO <sub>2</sub> / PbSe QD (Eg :1.0 eV)-EDT/	2.42	101 @ 370 nm	Haciefendioglu et al., 2021

(PbSe QD (eg: 1.0 eV) +PbSe NRs (eg:0.88 eV))-EDT/ PbSe QD (Eg :1.4 eV)- EDT/MoOx/Au		(3.8xEg of QDs)	
--	--	-----------------	--

Charge extraction applications from QDs are problematic since the architecture of QDs favors confinement of excitons in the cores for improved light emission, making it difficult to split excitons into charge carriers and then transfer them to the appropriate collectors. Designing hetero-structures in a variety of forms and geometries might provide better solutions for solar cell applications by increasing the possibilities of charge extraction and transport<sup>55</sup>. In this thesis, charge extraction and transport has been investigated by forming donor-acceptor type bulk nano-heterojunction solar cells based on PbSe NRs and PbSe QDs. Hacıfendioglu et al. have shown that using PbSe NRs and PbSe QDs based BNHJ platform increases the cell performance by effective charge extraction via TiO<sub>2</sub> as electron transport material, PbSe QDs front layer and non-annealed PbSe NRs and PbSe QDs based BNHJ platform. However, optimizing interfaces between PbSe NRs and PbSe QDs based BNHJ platform and ETL/ HTL by using ZnO as electron transport material, removing PbSe QDs front layer and annealing PbSe NRs and PbSe QDs based BNHJ platform increased the cell performance up to 4 % in terms of PCE. In addition, the cells were shown 100% EQE and 105% IQE which are the highest parameters for PbSe NRs and PbSe QDs based BNHJ platform based solar cells.



## CHAPTER 3

### EXPERIMENTAL

#### 3.1 Materials

All chemicals were of the highest purity available and used as delivered unless otherwise specified. All solvents were anhydrous and used as delivered.

Lead (II) acetate trihydrate ( $\text{Pb}(\text{C}_2\text{H}_3\text{O}_2)_2 \cdot 3(\text{H}_2\text{O})$ , 99.99%, Aldrich), selenium powder (200 mesh, 99.999%, Alfa Aesar), oleic acid (OA, 90%, Aldrich), trioctylphosphine (TOP, 90%, Aldrich), 1-Octadecene (ODE, 90%, Aldrich), diphenyl phosphine (DPP, 98%, Aldrich), lead(II) oxide, ( $\text{PbO}$ , 99.999%, Aldrich), squalene (90%, Aldrich), cadmium chloride ( $\text{CdCl}_2$ , 99.9%, Aldrich), tris(diethylamino)-phosphine (TDP, 90%, Aldrich), oleylamine (70%, Aldrich), tetradecyl phosphonic acid (TDPA, 98%, Alfa Aesar), tetrachloroethylene (TCE, 99%, Aldrich), 1,2-ethanedithiol (EDT, 98%, Aldrich), 1,3-Benzenedithiol (BDT, 98%, Aldrich), acetone (99.8%, Acros Organics), methanol (99.8%, Aldrich), butanol (99.8%, Aldrich), hexane (99%, Aldrich), 2-propanol (99.5%, Aldrich), acetonitrile, (99.8%, Aldrich), octane (99%, Aldrich), diethylzinc in hexane (1.0 M DEZn, Aldrich), tetrahydrofuran (THF,  $\geq 99\%$ , Aldrich), chloroform ( $\geq 99\%$ , Aldrich), 6,13-bis(triisopropylsilylethynyl)pentacene (TIPS-Pentacene,  $\geq 99\%$ , Aldrich), hexamethyldisilathiane ( $(\text{TMS})_2\text{S}$ , Aldrich).

#### 3.2 Synthesis

The synthesis of PbSe QDs and NRs were carried out by means of hot injection nanoparticle synthesis method using air-free Schlenk line techniques (see Figure 3.1). Purification steps of air sensitive PbSe QDs and NRs were performed in nitrogen filled glove box (GB) (see Figure 3.2).

### 3.2.1 Lead Selenide Quantum Dot Synthesis

The synthesis of oleic-acid-capped PbSe QDs were performed as described in the previous report<sup>2</sup>. Synthesis parameters for QDs with different band gaps is summarized in Table 3.1. Shortly, the Pb-oleate stock solution was prepared by mixing Pb(OAc)<sub>2</sub>·3H<sub>2</sub>O (1.30 g, 3.44 mmol), OA (2.68 ml, 8.412 mmol) and 24 mL ODE (75.8 mmol) in 100 mL three-necked flask. The magnetic stirrer in the flask was activated to ensure the materials distributed homogeneously in the mixture. The mixture was heated step by step up to 100 °C under vacuum see Figure 3.1 for an hour. The clear solution was then coordinated at 160°C under N<sub>2</sub> flow for four hours. Then Se stock solution was prepared in a nitrogen filled GB to prevent the oxidation of Se (see Figure 3.2). 1M TOP-Se was prepared by dissolving 0.7896 mg Selenium powder (10 mmol) in 10 ml TOP (22.4 mmol) at room temperature, under constant stirring. After transparent TOP-Se was formed, stock solution (10 mL) was mixed with 0.104 mL DPP (0.597 mmol) and rapidly injected to the Pb-oleate stock solution after lowering the temperature of the solution to the desired injection temperature. The injection was performed at 145°C, 110.4°C, and 80°C for PbSe QDs with 1.0 eV, 1.4 eV and 1.85 eV band gaps, respectively. Following the injection of the Se precursor, the color of the mixture immediately turned to black, indicating that the first nanocrystal formation has begun. After the desired growing time (100 s for 1.0 eV, 100 s for 1.4 eV and 120 s for 1.85 eV), reaction was quenched with the injection of 10 mL cold anhydrous hexane and placing the flask in a cold-water bath.



Figure 3.1. Schlenk line for the synthesis of air sensitive PbSe QDs and NRs.

Two consecutive purification and size-selective precipitation steps with anhydrous hexane/methanol and hexane/acetone solvent system were followed for the 1.4 eV PbSe QDs and 1.85 eV PbSe QDs: Step 1: hexane/methanol (1:1) and step 2: hexane/acetone (1:2.5). Two step anhydrous hexane/acetonitrile solvent system was used for the purification of 1.0 eV PbSe QDs: Step 1: hexane/acetonitrile (1:1), step 2: hexane/ acetonitrile (1:1), respectively. At each purification step the precipitated PbSe QDs were isolated by centrifugation at 5000 rpm for 5 min and quickly re-dispersed in hexane and precipitated with anti-solvent. The final PbSe QDs were kept in octane for thin film applications and in TCE for characterization studies. Before thin film applications, PbSe QDs were filtered with 0.22  $\mu\text{m}$  PTFE syringe filter.

Table 3.1 Synthesis parameters for QDs with different band gaps.

$E_g$ (PbSe QD)	OA/Pb	Se/Pb	$T_{inj}$	Growth time
1.0 eV	2.44	2.90	145°C	100 s
1.4 eV	2.44	2.90	110.4°C	100 s
1.85 eV	2.44	2.90	80°C	120 s



Figure 3.2. Nitrogen filled glove box to create an oxygen free environment for the processing of oxygen-sensitive materials.

### 3.2.2 Lead Selenide Nanorod Synthesis

The synthesis of oleic-acid-capped PbSe NRs were carried out according to the previous reports by Koh et al.<sup>56</sup> with some modifications<sup>28,31</sup>. Briefly, lead stock solution was prepared by mixing PbO (1.31 g, 5.88 mmol), OA (6 ml, 19 mmol) and 30 ml squalene (57.4 mmol) in 100 mL three-necked flask. The mixture was heated step by step up to 100 °C under vacuum using Schlenk line. Then transparent solution

was coordinated at 160 °C under N<sub>2</sub> flow for four hours. 18 mL of 1M TDP-Se, which was prepared by dissolving selenium powder (1.42 mg, 18 mmol) in TDP (18 ml, 65.7 mmol) inside a nitrogen filled GB, was rapidly injected to the Pb-oleate stock solution after lowering the temperature of the solution to the required injection temperature. The injection was performed at 173 °C and 170 °C for PbSe NRs with 0.88 eV and 0.95 eV band gaps, respectively. The color of the solution immediately turned to black which indicates the successful formation of the nanorods. The reaction was terminated at the end of two minutes by the injection of 20 mL of cold anhydrous hexane and placing the flask in a cold-water bath. After the reaction was complete, anhydrous hexane/isopropanol solvent system was used for the size-selective precipitation of the NRs. Ultimately, precipitated NRs were isolated with centrifugation at 5000 rpm for 5 minutes and re-dispersed in hexane. Precipitation and re-dispersion steps were repeated two times; step 1: hexane/ isopropanol (1:2) and step 2: hexane/ isopropanol (1:1). The final PbSe NRs were filtered with 0.22 µm PTFE syringe filter and kept in octane for thin film applications and in TCE for the characterization studies.

For the synthesis passivated PbSe NRs (SynP-NRs), CdCl<sub>2</sub> solution was prepared from CdCl<sub>2</sub> (0.30 g, 1.63 mmol) and TDPA (26.73 mg, 0.096 mmol) in oleylamine (5ml) and degassed for 16 h. at 100°C. CdCl<sub>2</sub> solution (1.5 ml) is injected at 100°C at the end of growth period of PbSe NRs. The temperature of the solution is gradually decreased from 100 to 65 ± 5°C in 10 s then the reaction is terminated via ice cold hexane injection and placing a water bath under the flask.

### **3.2.3 Lead Sulfide Quantum Dot Synthesis**

PbS QDs having 1.3 eV bandgap was synthesized according to literature modified method<sup>57,58</sup>. PbO (0.4528 g, 2.0277 mmol), oleic acid (1.51 mL, 4.7578 mmol) and 1-octadecene (17.99 mL) was mixed in a three-neck flask and degassed up to 90°C then heated under vacuum at 100°C for two hours until the clear solution formation. Then reaction medium was kept under N<sub>2</sub> stream and heated to 160°C for 2 hours to coordinate Pb and oleate groups to form Pb-oleate complex. Then, the temperature

was gradually lowered to the injection temperature of 125°C. To prepare sulfur precursor, 10 mL 1-octadecene (dried under vacuum at 80°C for 16 hours and stored in the GB) is mixed with hexamethyldisilathiane (0.21 mL, 0.9956 mmol) at room temperature inside the GB. This solution was rapidly injected to the Pb-oleate solution at 125°C. This syringe and anything that is contaminated with hexamethyldisilathiane was quickly dipped to bleach solution before disposing it to the sharps bin. Nucleation reaction had started in 5 s after the injection of the hexamethyldisilathiane solution. At the end of 20 s growth period, the reaction was terminated by using an ice bath. The crystals were transferred first to a Schlenk tube using a stainless steel cannula and then to the GB for purification steps. Obtained crystals were purified two times using hexane/acetone solvent/anti solvent pair followed by centrifugation at 5000 rpm for 5 minutes; step 1: hexane/acetone (1:4), step 2: hexane/acetone (1:1). Vacuum dried precipitate was dispersed in octane and filtered through 0.22 µm PTFE syringe filter for solar cell applications and characterization steps.

### **3.2.4 Zinc Oxide Nanoparticle Synthesis**

ZnO NPs were synthesized following a method adapted from that reported by Davis et al.<sup>3</sup>. Briefly, the zinc oxide precursor was prepared by diluting 250 µl of diethylzinc (DEZn) in hexane (1 M) in 750 µl anhydrous tetrahydrofuran (THF) under vigorous stirring. It was prepared in nitrogen filled GB to prevent ignition of diethylzinc. ZnO NPs were prepared fresh and filtered with a 0.45 µm PVDF syringe filter before use.

### **3.3 Material Characterization / Instrumentation**

#### **3.3.1 Absorption Spectroscopy**

Absorption spectra of NPs suspended in TCE (using an airtight quartz cuvette) or coated as thin film on quartz/glass substrates were recorded using a Shimadzu 3600 plus UV-Vis-NIR spectroscopy system. The samples were prepared in an inert environment provided by the nitrogen filled GB.

#### **3.3.2 Transmission Electron Microscopy (TEM)**

TEM measurements were done using a Jem Jeol 2100F 200kV high-resolution transmission electron microscopy (HRTEM) operating at 80-200 kV with Schottky type field emission gun as a source of electron. Samples for TEM imaging were prepared onto 200 Mesh carbon coated TEM grids by drop-casting a dilute solution of NPs in TCE and allowing solvent to evaporate at room temperature. GATAN, Orius SC1000 2 camera was used as the CCD camera.

#### **3.3.3 UV Photoelectron Spectroscopy (UPS)**

UPS measurements were done using PHI 5000 VersaProbe in ultrahigh vacuum conditions ( $10^{-10}$  mbar) with monochromatic HeI UV source (21.2 eV). The low energy cut-off was determined by biasing samples at -7.00 V. Samples were prepared by spin coating OA-capped NPs onto a precleaned Si/Cr (10 nm)/Au (150 nm) substrates which were prepared at METU MicroElectroMechanical Systems (MEMS) center. Since the samples were air sensitive, they were prepared in nitrogen filled GB and kept in the air-tight tube till the loading to the instrument. An UPS spectrum of 0.95 eV PbSe NRs and three main steps used to determine the valence and conduction band energies are represented in Figure 3.3. The difference in energy level between the input photon energy (21.2 eV) and the high binding energy edge (shown in Figure 3.3. UPS spectrum of 0.95 eV PbSe NR Figure 3.3) was used to

calculate the Fermi level (step 1), referenced to vacuum. The low binding energy edge (as indicated in Figure 3.3) was used to calculate the minimum valence band energy. The minimum conduction band energy was calculated by subtracting the minimum valence band energy from the band gap determined from the peak point of the absorption spectrum<sup>3,59</sup>.

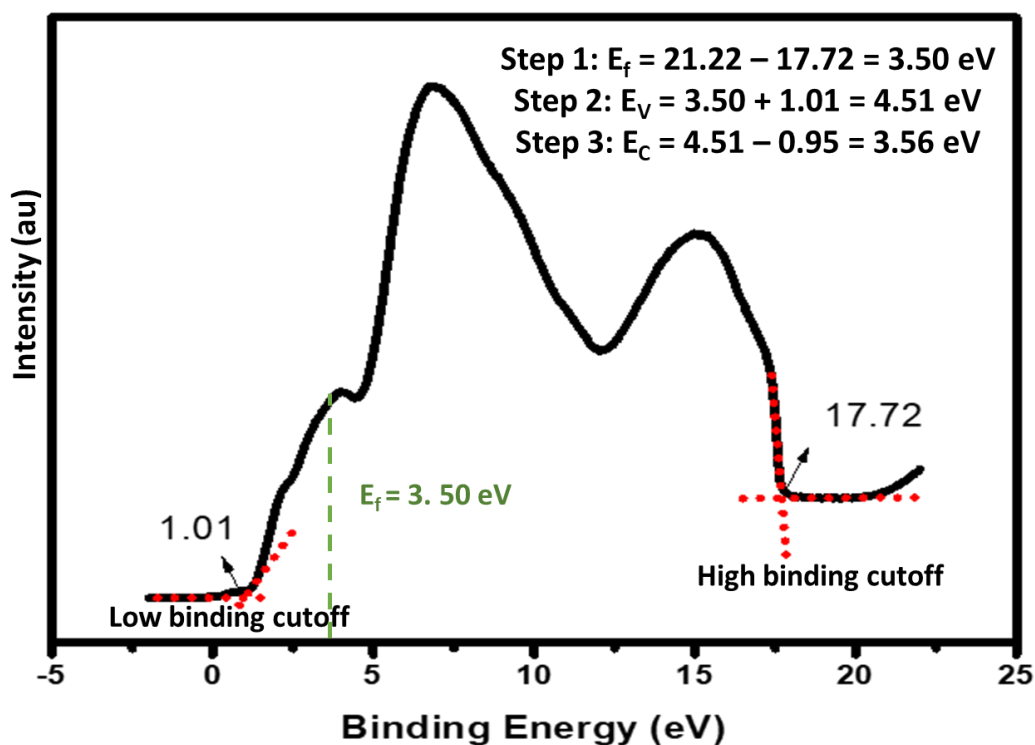


Figure 3.3. UPS spectrum of 0.95 eV PbSe NR.

### 3.4 Solar Cell Fabrication

Solar cell fabrication steps are schematically represented in Figure 3.4. Indium tin oxide (ITO) patterned glass substrates, purchased from Psiotec, were sequentially cleaned by sonication in acetone, isopropyl alcohol, hellmanex III, and deionized water for 15 minutes. Then, substrates were dried under nitrogen stream, and left in the oven with the temperature set at 100°C for at least 3 hours.

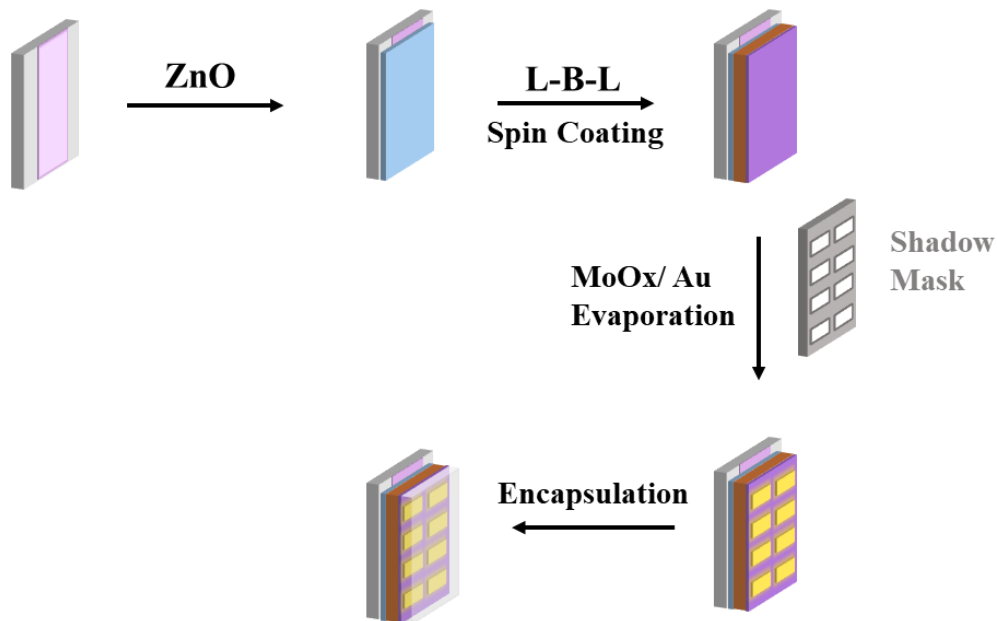


Figure 3.4. Schematic representation of solar cell fabrication process.

ZnO electron transporting layer was coated onto the ITO patterned glass substrates right after etching them with air plasma for 30 minutes to remove any organic residues. ZnO precursor mixture was filtered through a 0.45  $\mu\text{l}$  pore-sized PTFE syringe filter and spun on to ITO substrates at 6000 rpm for 35 s under atmospheric conditions. These ZnO-covered substrates were annealed at 130°C for 30 minutes on a hot plate in an ambient environment. The ITO/ZnO substrates were quickly transferred to nitrogen-filled GB to spin-coat the active layers. Spin coating parameters and the characteristics of the NP solutions used throughout this thesis are summarized in Table 3.2.

Table 3.2 Spin coating parameters and the characteristics of the NP solutions

NP	Concentration/Solvent	GB/Ambient	Spin Coater Parameters
ZnO	0.25 M /THF	Ambient	6000 rpm-35 s
PbSe QDs	30 mg.ml <sup>-1</sup> /octane	GB	1500 rpm-2 s 2500 rpm-10 s
PSe NRs	30 mg.ml <sup>-1</sup> /octane	GB	1500 rpm-2 s 2500 rpm-10 s
QD-NR	25 mg.ml <sup>-1</sup> /octane	GB	1500 rpm-2 s 2500 rpm-10 s
PbS QDs	50 mg.ml <sup>-1</sup> /octane	GB	1500 rpm-2 s 2500 rpm-10 s
TIPS-Pentacene	2.50 mg.ml <sup>-1</sup> / chloroform	GB	1500 rpm-50 s
EDT	(0.02 v% / acetonitrile)	GB	1500 rpm-2 s 2500 rpm-10 s
BDT	(0.20 v% / acetonitrile)	GB	1500 rpm-2 s 2500 rpm-10 s

NR/QD blends were prepared by mixing PbSe NRs (50 mg.ml<sup>-1</sup> in octane) and PbSe QDs (50 mg.ml<sup>-1</sup> in octane) in equal volumes. NR/QD blends (25 mg.ml<sup>-1</sup>) or PbSe-QDs dissolved in octane (30 mg.ml<sup>-1</sup>) were deposited in a layer-by-layer (L-B-L) approach on top of the ZnO ETL at 1500 rpm (2 s) and 2500 rpm (10 s) inside the GB.

For the L-B-L spin coating process, schematically represented in Figure 3.5. PbSe NRs/ QDs were first treated with EDT (0.02 v% in acetonitrile (ACN)) for 30 s and then rinsed with ACN (3 times) and octane to remove the excess ligand and un-exchanged nanoparticles, respectively. For the BDT treatment, PbSe NRs/ QDs were first treated with BDT (0.20 v% ACN) for 30 s and then rinsed with ACN (3 times)

and octane to remove the excess ligand and un-exchanged nanoparticles, respectively. Active layers were annealed at 70°C for 5 minutes before HTL coating process. Finally, the substrates were loaded into a thermal evaporator to evaporate MoOx (7 nm) and Au (100 nm) or Ag (100 nm) at a pressure of 10<sup>-6</sup> Torr. A shadow mask with an active area of 4.5 mm<sup>2</sup> was used to define the active area of the solar cells. Finally, the cells were encapsulated using a transparent epoxy resin and glass slides.

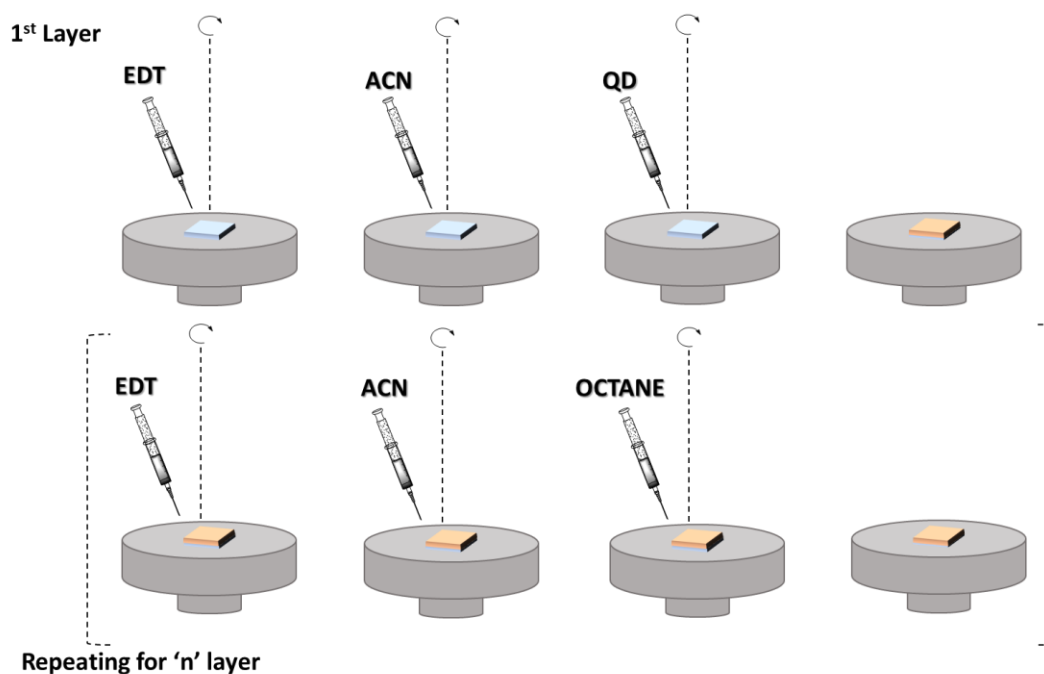


Figure 3.5. Schematic representation of L-B-L spin coating process.

Notation of cell architecture and explanations of the abbreviations used throughout this thesis is represented below. For all the cells, ITO and ZnO were used as the substrate and ETL, respectively. The cell architecture indicates the NP type and bandgap.

ITO / ZnO / (PbSe NR<sub>0.90 eV</sub> + PbSe QD<sub>1.0 eV</sub>) - EDT(2L) / Tips-Pentacene(1L) / MoO<sub>x</sub> / Au



Type of the ligand (ethane-1,2-dithiol or benzene-1,3-dithiol), used to replace the oleate ligands present in as synthesized NPs, was noted in the notation. In addition, the number of spin-casted layers was shown in the parentheses, and each slash represents the layer type separation. In all cells, MoO<sub>x</sub> was used as a hole extraction layer from the active layer to the Au (or Ag) metal cathode.

### 3.5 Solar Cell Characterization

#### 3.5.1 Current-Voltage Measurement

I-V measurements were performed by using a solar simulator and a Keithley 2400 source measuring equipment under ambient conditions. The measurement was conducted using an ABET SunLite solar simulator (ASTM Class A stability) with AM1.5 G sun irradiation across a 50x50 mm area and a 100 W Xe arc lamp (PN: 13013). Solar simulator was calibrated by monocrystalline silicon reference cell (Newport, 91150V Reference Cell). Reported results were averaged over 4-6 cells with standard deviation. J<sub>SC</sub>, V<sub>OC</sub>, FF and PCE values of the cells with maximum PCEs were indicated in parentheses.

#### 3.5.2 Quantum Efficiency Measurement

A Newport QUANTX-300 apparatus represented in Figure 3.6-a was used to evaluate the external quantum efficiency (EQE) and internal quantum efficiency (IQE) of the solar cells. The measurements were conducted outside at 20-28°C with an 85 mm working distance. Measurements were conducted on cells attached to a

test holder as indicated in Figure 3.6-b. The current generated by the test solar cell (603415 QUANTX 300), represented in Figure 3.6-c, was compared to that generated by the calibrated photodiodes with a known EQE for the EQE and IQE measurements. The incoming white light source (100 W Xenon lamp) was filtered out and its central wavelength was tuned throughout a desirable range using an Oriel Monochromator (CS130). The calibrated reference detector for 325-1800 nm range was a silicon-germanium detector (PN: 603621, see Figure 3.6-d) which was calibrated at NRC (Newport Research Center). For the wavelengths between 300 nm - 330 nm, 330 nm - 340 nm, and 350 nm - 1800 nm, EQE was measured with an uncertainty of 25%, 7%, and 3%, respectively. The High and Low calibrated reflectance standards (Newport IQE200B (603414 QUANTX-300 Specular Reflectance Standard) for the IQE tests are represented in Figure 3.6-e. Before each measurement, the spectral response was compared to that of the test cell with an uncertainty of 0.5 % of the measured value.

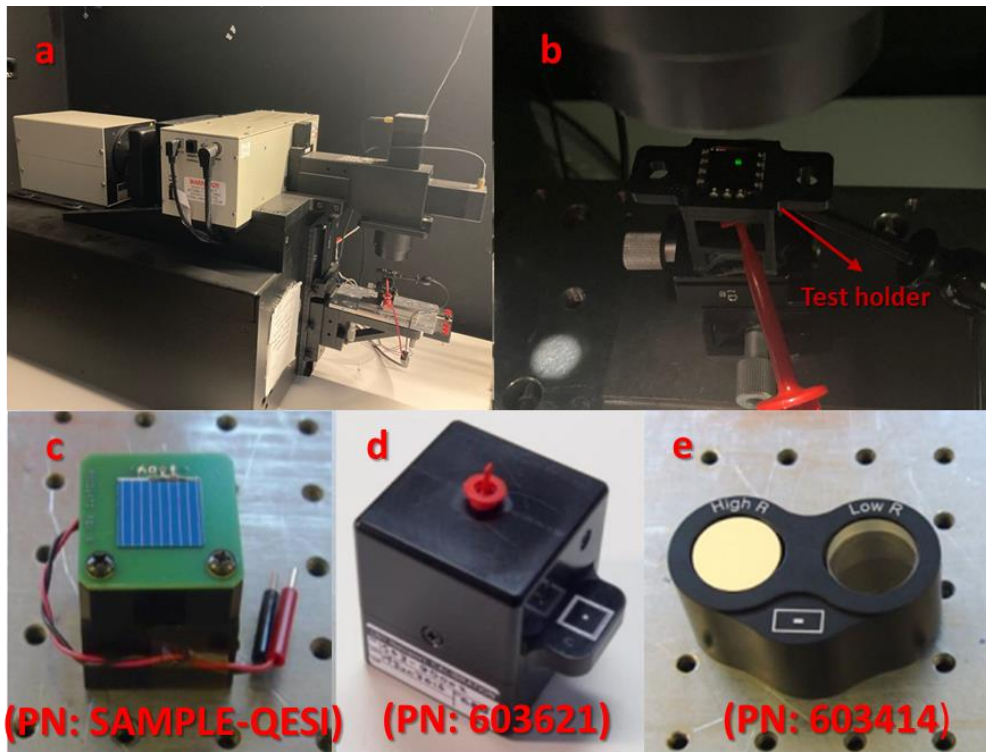
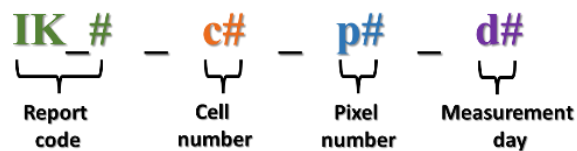


Figure 3.6. External/internal quantum efficiency measurement setup and calibration standards. **a)** Newport QUANTX-300 apparatus. **b)** Ongoing measurement on a solar cell attached to a test holder. **c)** Silicon test cell. **d)** Calibrated silicon-germanium reference detector. **e)** High and Low calibrated reflectance standards for the IQE tests.

Notation of experimental code used in results part and explanations of the abbreviations are represented below.



## CHAPTER 4

### RESULTS AND DISCUSSION

#### 4.1 Characterization of PbSe QDs/NRs/SynPNRs and PbS QDs

To investigate the role of QDs and NRs in solar cells design based on MEG process and optimize the cell performance, various QDs and NRs were synthesized throughout this thesis. PbS QDs with 1.3 eV band gap, PbSe QDs with varying band gaps (1.0 eV, 1.4 eV and 1.85 eV) and PbSe NRs with 0.95 eV band gap were synthesized according to our previous reports with some modifications<sup>31,56,60</sup>. Band gap of the QDs and NRs were controlled via varying the injection temperature and time<sup>3</sup>. After purification steps, the final PbSe QDs and NRs were dispersed in octane for thin film applications and in TCE for characterization studies. Absorbance spectra of the dilute solutions of OA capped PbS QDs, PbSe QDs and NRs in octane and of the thin films on quartz spectrosls were represented in Figure 4.1. Optical band gaps were calculated from the peak point of the absorbance spectra of the OA capped QDs.

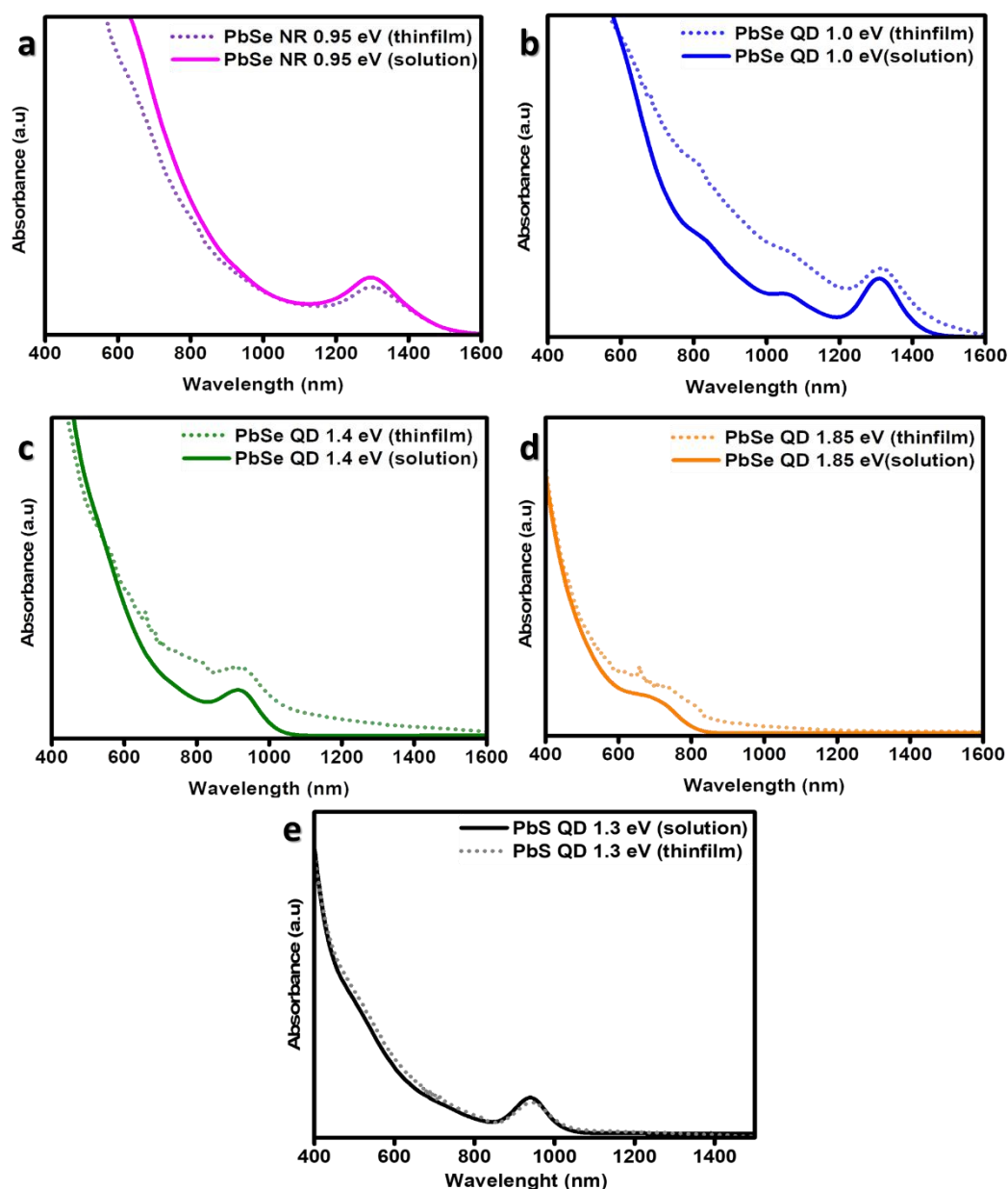


Figure 4.1. Absorbance spectra of the QDs and NRs in octane and thin film **a)** PbSe NRs (0.95 eV), **b)** PbSe QDs (1.0 eV), **c)** PbSe QDs (1.4 eV), **d)** PbSe QDs (1.85 eV) and **e)** PbS QDs (1.3 eV).

Solar cell performance and photophysical properties of light absorbing BNHJ layer can be altered by modulating the electron donor, electron acceptor units. To investigate the donor -acceptor properties of QDs and NRs three different donor-acceptor units were formed by blending PbSe QDs of various band gaps with 0.95

eV NRs in 1:1 ratio in weight. For Bulk-1, 1.0 eV QDs were blended with 0.95 eV NRs where NRs and QDs act as donor and acceptor, respectively. For Bulk-2, 0.95 eV NRs were blended with 1.4 eV QDs where conduction bands of the two nanoparticles become equal. Finally, 0.95 eV NRs were blended with 1.85 eV QDs for Bulk-3 where 1.85 eV QDs donor conduction band level is higher in energy than that of 0.95 eV NRs acceptor. Absorbance spectra of the dilute solutions of Bulk-1, Bulk-2 and Bulk-3 in octane are represented in Figure 4.2-a, b and c.

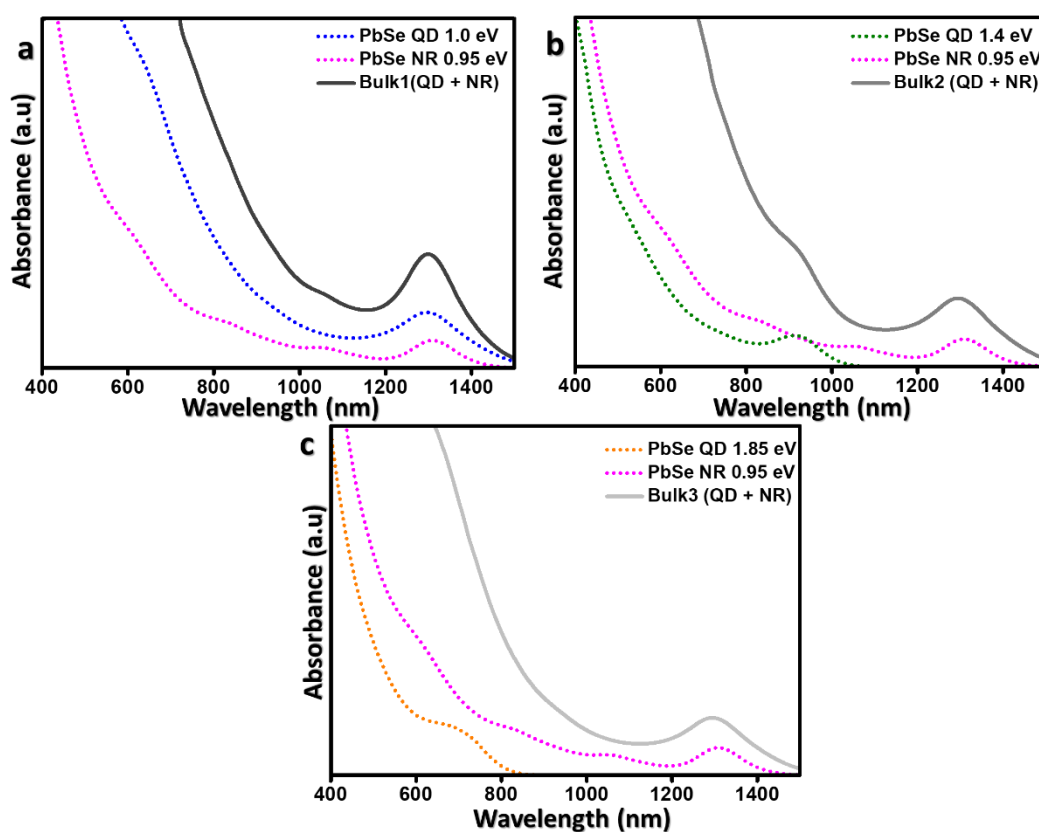


Figure 4.2. Absorbance spectra of the three different blends. **a)** Bulk-1: PbSe QDs (1.0 eV) + PbSe NRs (0.95 eV). **b)** Bulk-2: PbSe QDs (1.4 eV) + PbSe NRs (0.95 eV). **c)** Bulk-3: PbSe QDs (1.85 eV) + PbSe NRs (0.95 eV).

TEM measurements were performed to investigate the shape and morphology of QDs, NRs and Bulk-1, Bulk-2 and Bulk-3 bulk nano-heterojunction thin films.

Figure 4.3-a shows the TEM image of EDT capped NRs with 0.95 eV band gap. The aspect ratio of the NRs was determined as 10.29 (diameter, D: 3.1 nm and length, L: 31.9 nm) which is in line with previous studies<sup>31</sup> where the diameter and length distribution of NRs were reported as 3.1 nm and 31.9 nm, respectively. Figure 4.3-b represents the TEM image of EDT capped 1.0 eV PbSe QDs. In line with the previous studies where the diameter of PbSe QDs with 1.0 eV band gap was reported as 3.3 nm<sup>61</sup>, the size of 1.0 eV was determined as 3.3 nm. Figure 4.3-c-e represent the TEM images of Bulk-1, Bulk-2 and Bulk-3 where the nanoparticles are EDT capped. In line with the previous studies, the diameters of 1.4 eV and 1.85 eV QDs were determined as 2.9 nm<sup>62</sup> and 2.1 nm<sup>63</sup>, respectively. Size statistics studies on TEM images were performed using ImageJ analysis program<sup>81</sup>. Band gaps as well as sizes of the NPs were summarized in Table 4.1. As expected, size of QDs were decreased while band gap increasing as seen in TEM images and summarized in Table 4.1.

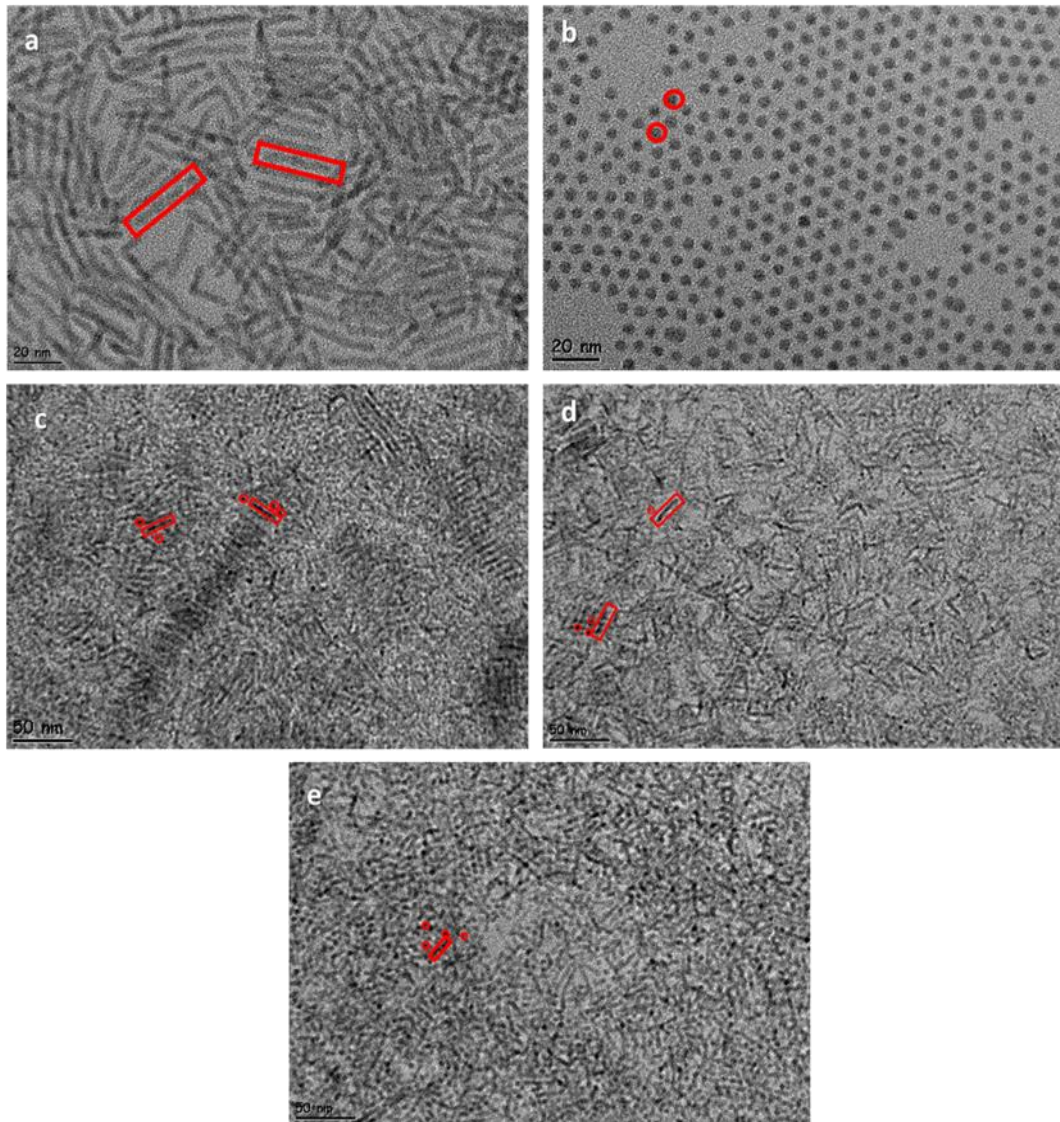


Figure 4.3. TEM images of **a)** EDT capped PbSe NRs with band gap 0.95 eV (scale bar: 50 nm), **b)** EDT capped PbSe QDs with band gap 1.0 eV (scale bar: 20 nm), **c)** Bulk-1: PbSe NRs with 0.95 eV with 1.0 eV QDs (scale bar: 50 nm). **d)** Bulk-2: PbSe NRs with 0.95 eV with 1.4 eV QDs (scale bar: 50 nm), **e)** Bulk-3: PbSe NRs with 0.95 eV with 1.85 eV QDs (scale bar: 50 nm)

Table 4.1 Band gap and size properties (average diameter (D) and average length (L)) of PbSe QDs and NRs used in solar cell studies.

	<b>E<sub>g</sub><sup>a</sup></b>	<b>D<sup>b</sup></b>	<b>L<sup>b</sup></b>
PbSe QDs	1.0 eV	3.3 ± 0.5	-
PbSe QDs	1.4 eV	2.9 ± 0.3	-
PbSe QDs	1.85 eV	2.1 ± 0.2	-
PbSe NRs	0.95 eV	3.1 ± 0.4	31.9 ± 7.1

<sup>a</sup> Band gaps were calculated from the absorption peak wavelength of the QDs and NRs in solution.

<sup>b</sup> Average diameter (D) and length (L) were determined from the TEM images of at least 50 QDs/NRs by using ImageJ analysis program.

UPS measurement was conducted to determine the band edge energies with respect to vacuum in PbSe QDs, NRs and Bulk-1. UPS studies were also performed for TIPS-Pentacene films, which was used as HTL in this thesis, to make a comparison of our UPS facility with other research groups. Optical band gaps, conduction, and valence band energy levels of all synthesized and used materials were summarized in the Table 4.2. Surface passivation of the NRs caused a shift of the valence/conduction bands toward lower energy as shown in Table 4.2 and Figure 4.4. Valence band energy levels of the PbSe QDs and SynP-PbSe NRs were reported as -5.23 and -4.83 eV, respectively. According to Table 4.2, valence band energy levels of QDs and SynP-NRs are in line with the studies reported before<sup>64</sup> where it was reported as -5.2 and 4.8 eV, respectively. The valence/conduction bands of TIPS-Pentacene were found as -4.9 eV and -3.1 eV, respectively, which is also in line with the previous studies<sup>65</sup> (VB: -4.9 eV and CB: -3.1 eV). Valence band of PbS QD was adapted from the literature.

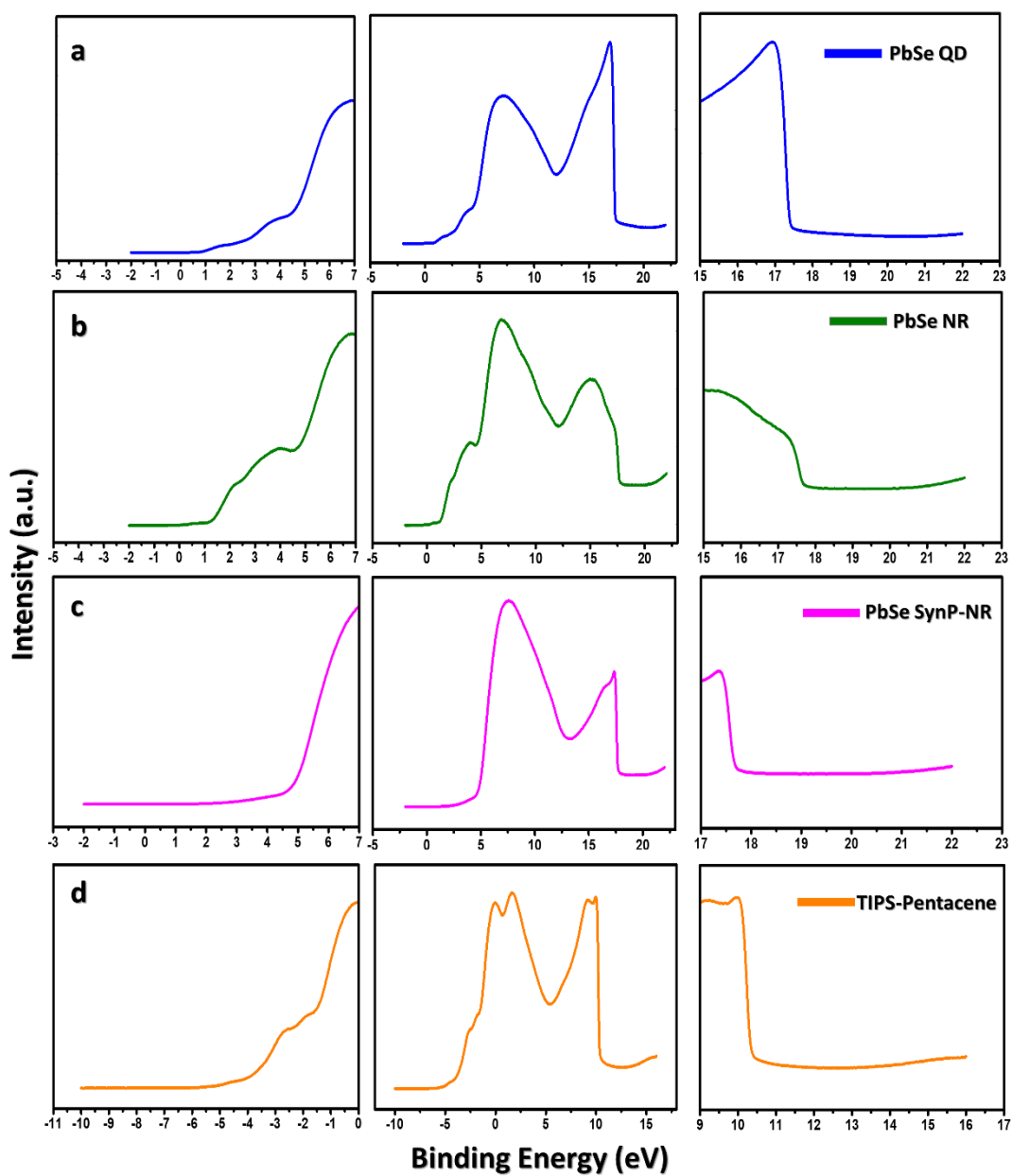


Figure 4.4. UPS measurements of EDT capped **a)** PbSe QDs (1.0 eV), **b)** PbSe NRs (0.95 eV), **c)** PbSe SynP-NRs (0.88 eV) and **d)** TIPS-Pentacene.

Table 4.2 Band edge energies of the EDT capped PbSe QDs, PbSe NRs, PbS QDs and TIPS-Pentacene with respect to vacuum.

	Optical $E_G^a$ (eV)	$E_v^b$ (eV)	$E_c^b$ (eV)
PbSe QD <sub>1.0 eV</sub>	1.0	-5.23	-4.23
PbSe QD <sub>1.4 eV</sub>	1.4	-5.23	-3.83
PbSe QD <sub>1.85 eV</sub>	1.85	-5.23	-3.38
PbSe NR <sub>0.95 eV</sub>	0.95	-4.51	-3.58
SynP-PbSe NR <sub>0.95 eV</sub>	0.95	-4.83	-3.88
TIPS-Pentacene	1.8	-4.90	-3.10
PbS QD <sub>1.3 eV<sup>c</sup></sub>	1.3	-5.00	-3.70

<sup>a</sup> Determined from the absorption spectra;

<sup>b</sup> Determined from UPS measurements conducted at METU Central Laboratories;

<sup>c</sup> Valence/conduction band energies were adapted from literature<sup>66</sup>.

The UPS spectra of Bulk-1 where the NPs are EDT capped, is represented in Figure 4.5.

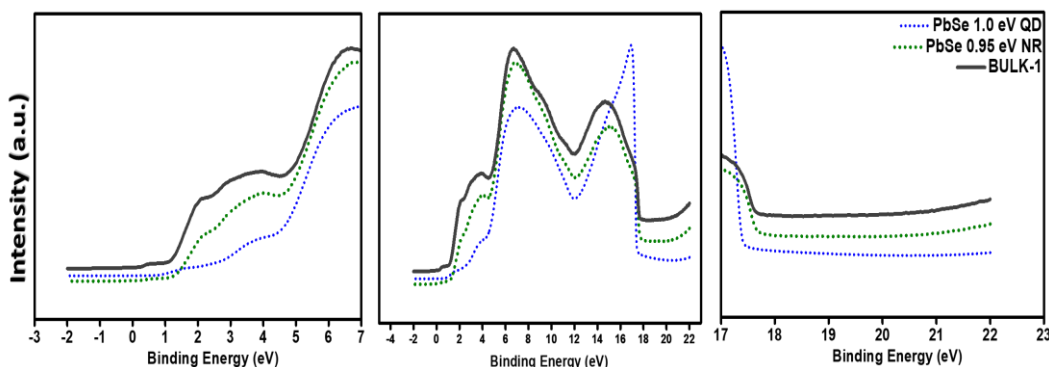


Figure 4.5. UPS measurements of Bulk-1, where the NPs are EDT capped.

## 4.2 Solar Cell Application

Solar cells fabricated in this thesis are composed of main components like active layer, electron transport layer, hole transport layer and metal electrodes. Electrons and holes are created as a result of the light being absorbed by the active layer. The electron and hole transport layers subsequently deliver these load carriers to the electrodes. The active layer, the electron transport layer, and the hole transport layer are particularly vital to the construction of solar cells due to their crucial roles in the cell performance.

Generally solar cells have conventional cell structure fabricated by subsequently coating a hole transport layer (HTL), an active layer, an electron transport layer (ETL), and a low function metal layer on transparent electrode (ITO: indium tin oxide, FTO: fluoride tin oxide) coated glass substrate.

In contradistinction to the conventional solar cells, for the bulk nano-heterojunction solar cells fabricated in this thesis, inverted solar cell structure was utilized by subsequently coating an electron transport layer, an active layer, a hole transport layer, and a high function metal layer on the transparent electrode (ITO, FTO) coated glass substrate. The essential reason behind utilizing the inverted structure is to provide maximum gain from the whole solar spectrum by allowing high-energy photons to reach and absorbed by the active layer.

In this study, ZnO were used as the transparent electron transport layer. BNHJ layers prepared by blending PbSe NRs with PbSe QDs were used as the active layer. For the hole transport layer, various materials such as PbSe QD, PbS QD and TIPS-Pentacene were used. These components were optimized to enhance the cell performance.

#### 4.2.1 Effect of the Front QD Layer

Hacıfendioglu et al. reported solar cell with a QD front layer coated right before the light absorbing BNHJ active layer. The cells were consisting of TiO<sub>2</sub> as ETL, one layer of PbSe QD<sub>1.06 eV</sub> as front layer, two layers of BNHJ layers (prepared by blending PbSe QD<sub>1.06 eV</sub> with SynP-NR<sub>0.95 eV</sub>) as active layer, PbSe QD<sub>1.38 eV</sub> as HTL and Ag as a back contact. Power conversion efficiency of the champion cell was reported as 2.05%. To investigate whether the limited cell performance is due to the front QD layer, cells with and without front layer were fabricated and cell performances were compared as represented in Figure 4.6-a and summarized in Table 4.3. one with front QD layer, other without front QD layer. The architectures of the cells were shown in the Figure 4.6-a. The cells were consisting of ZnO as ETL, two layers of Bulk-1 (PbSe QD<sub>1.0 eV</sub> + SynP-NR<sub>0.95 eV</sub>), PbSe QD<sub>1.4 eV</sub> as HTL and Ag as a back contact.

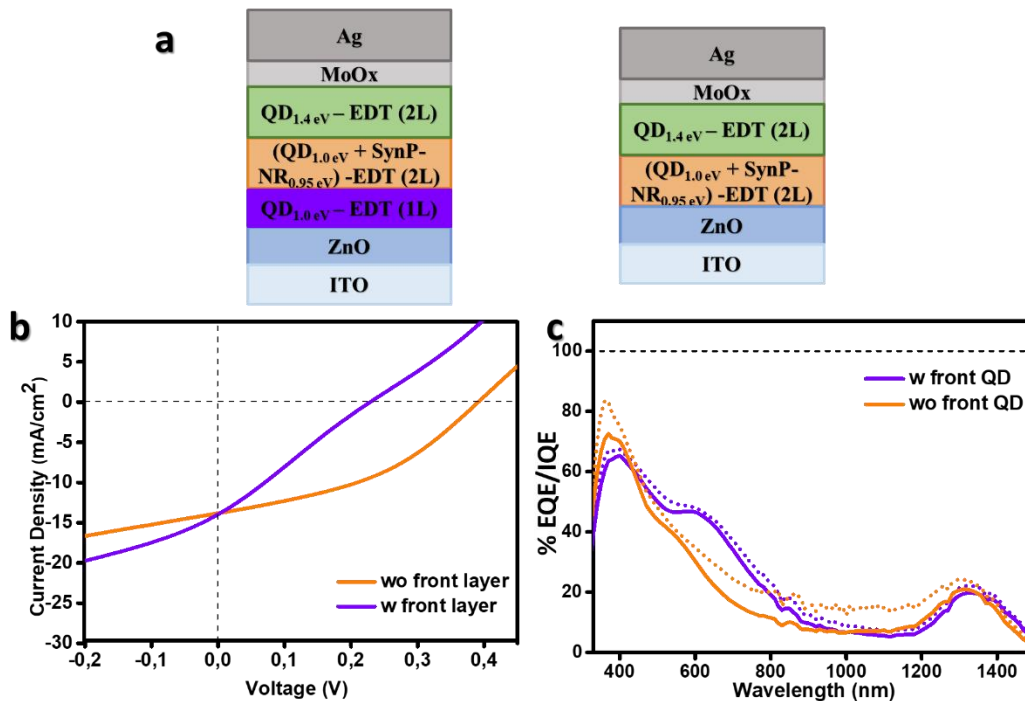


Figure 4.6. Role of PbSe QD<sub>1.0 eV</sub> front layer on the photovoltaic performance of the solar cell. **a)** Schematic representation of cell architectures. **b)** I-V characteristics and, **c)** EQE/IQE spectra.

I-V characteristics of the cells are shown in Figure 4.6-b and performance parameters are summarized in Table 4.3. Although front QD layer does not have a significant impact on  $J_{sc}$  values, a dramatic increase in  $V_{oc}$  (from 0.23 V to 0.39 V) was reported for the cells where front QD layer was removed. In addition to  $V_{oc}$ , increase in FF from 25.57 to 40.61 contributed to the improvement in PCE. The major result from the modification of the front QD layer was noted for the EQE/IQE measurements. As seen in the Figure 4.6-c, EQE of the cell at 400 nm increased from 62 to 72 and IQE from 65 to 82 nm when the front QD layer is removed. As a result, modification of the cell architecture by removing the QD front layer was noted as a promising step to increase EQE at wavelengths where the MEG is expected to take place.

Table 4.3 Effect of PbSe QD<sub>1.0 eV</sub> front layer on solar cell characteristics.

<b>Front layer</b>	<b>Jsc (mA.cm<sup>-2</sup>)</b>	<b>Voc (V)</b>	<b>FF</b>	<b>PCE (%)</b>	<b>Jsc<sup>EQEa</sup> (mA.cm<sup>-2</sup>)</b>	<b>Exp code</b>
with front layer <sup>b</sup>	12.50 ±0.15 (13.96)	0.22 ±0.01 (0.23)	26.04 ±0.10 (25.57)	0.79 ±0.01 (0.81)	14.24	BB_7_ c5_p4_ d14
without front layer <sup>c</sup>	13.30± 0.10 (13.80)	0.37 ±0.01 (0.39)	39.48 ±0.10 (40.61)	1.97 ±0.02 (2.17)	11.29	BB_7_ c8_p7_ d20

<sup>a</sup> Theoretical  $J_{sc}$  calculated from the EQE spectrum.

<sup>b</sup> Cell architecture: ITO / ZnO / PbSe QD<sub>1.0 eV</sub> -EDT (1L) / Bulk- EDT (1L) / PbSe QD<sub>1.4 eV</sub> -EDT (2L) / MoOx / Ag where BULK: (PbSe QD<sub>1.0 eV</sub> + SynP-PbSe NR<sub>0.95 eV</sub>).

<sup>c</sup> Cell architecture: ITO / ZnO / Bulk-EDT (1L) / PbSe QD<sub>1.4 eV</sub> -EDT (2L) / MoOx / Ag where BULK: (PbSe QD<sub>1.0 eV</sub> + SynP-PbSe NR<sub>0.95 eV</sub>).

#### 4.2.2 Effect of Annealing of the BNHJ Active Layer

In the literature, many studies were conducted to investigate the effect of thermal annealing on the active layer morphology and cell performance<sup>67–69</sup>. It has been observed that there is an increase in cell performances as a more uniform morphology is obtained by thermal annealing of the active layer<sup>69</sup>. In the light of these information, effect of thermal annealing of active layer were investigated for BNHJ solar cell. Two different cells were fabricated one with thermal annealing of active layer at 70°C for 5 minutes, other without thermal annealing. The cells were consisting of ZnO as ETL, 1 layer PbSe QD<sub>1.0 eV</sub>, 2 layers of blend of PbSe QD<sub>1.0 eV</sub> with SynP-NR<sub>0.95 eV</sub> as active layer, PbSe QD<sub>1.4 eV</sub> as HTL and also Ag as a back contact.

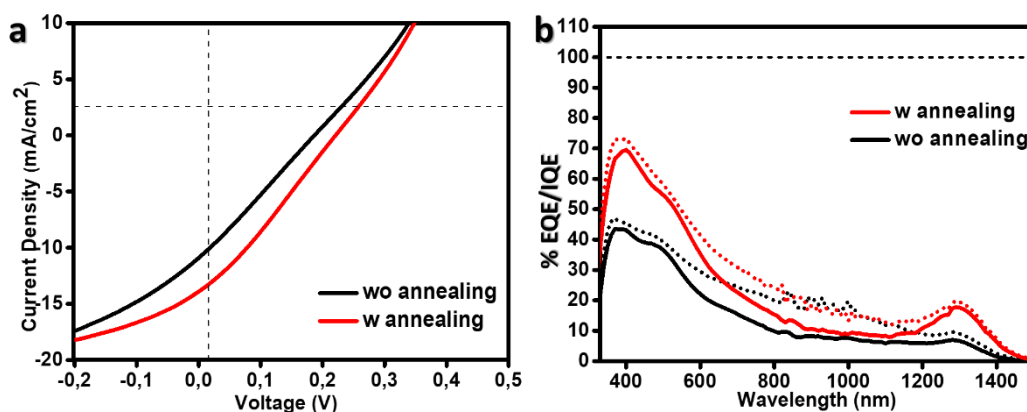


Figure 4.7. Role of annealing of light absorbing layer on the photovoltaic performance of the solar cell. **a)** I-V characteristics and, **b)** EQE/IQE spectra.

I-V characteristics of the cells were shown in Figure 4.7-a and performance parameters of the cells were summarized in Table 4.4.  $J_{sc}$  and  $V_{oc}$  increased by the annealing of the active layer. Increasing of the  $J_{sc}$ ,  $V_{oc}$  and the FF caused enhancement of PCE of the cells. Maximum performance of 0.86% was obtained for the cells with annealing of active layer where  $V_{oc}$ , FF and  $J_{sc}$  were recorded as 0.23 V, 31.11% and 12.75 mA.cm<sup>-2</sup>, respectively.

Table 4.4 Effect of annealing of the light absorbing active layer on the cell performance.

Annealing	Jsc (mA.cm <sup>-2</sup> )	Voc (V)	FF	PCE (%)	Jsc <sup>EQEa</sup> (mA.cm <sup>-2</sup> )	Exp code
wo <sup>b</sup>	9.45 ±1.38 (10.92)	0.16 ±0.02 (0.18)	26.05 ±0.69 (24.89)	0.38 ±0.10 (0.53)	8.24	BB_ 7_c2 _p8 _d6
w <sup>b</sup>	13.34 ±0.43 (12.75)	0.18 ±0.03 (0.23)	26.08 ±1.08 (31.11)	0.64 ±0.13 (0.86)	13.11	BB_ 7_c9 _p- d6

<sup>a</sup> Theoretical J<sub>SC</sub> calculated from the EQE spectrum.

<sup>b</sup> Cell architecture: ITO / ZnO / PbSe QD<sub>1.0 eV</sub>-EDT (1L) / Bulk - EDT (1L) / PbSe QD<sub>1.4 eV</sub> - EDT (2L) / MoO<sub>x</sub> / Ag where BULK: (PbSe QD<sub>1.0 eV</sub> + SynP-PbSe NR<sub>0.95 eV</sub>)

As seen in the Figure 4.7-b, QE of the cell showed increase in the whole spectrum region. The EQE value measured around 1300 nm increased from 10% to 20% with thermal annealing. This 2-fold increase in the EQE observed in the area absorbed by the nanorods was proof that enhancement the morphology with annealing. Annealing also led to enhancement in photocurrent production in UV region where the MEG is expected to take place.

### 4.2.3 Optimization of the ZnO ETL

A suitable ETL should have some characteristics like having high electron mobility being transparent in visible and near infrared spectrum region and having a compatible energy levels that allows efficient extraction of the electrons by the conduction band and blocking of the holes by the valence band<sup>70</sup>. To collect and transport electrons effectively and enhance the cell performance parameters such as J<sub>SC</sub> and FF, ETLs must have relatively high electron mobility<sup>71</sup>. Having a wide band

gap (3.3 eV), being transparent, having high electron mobility ( $166 \text{ cm}^2 \text{ V.s}^{-1}$ ) and high exciton binding energy (60 meV) have greatly triggered the employment of ZnO as ETL<sup>72</sup>. According to the literature, ZnO synthesized by DEZn are the most common used ETL for the MEG based solar cell studies<sup>3,47,73</sup>. Therefore, in order to enhance the cell performance and to exceed the 100% external quantum efficiency, electron transporting ZnO layer was optimized for the BNHJ solar cells.

The annealing process is a crucial parameter for the formation of ZnO crystals. For the ZnO ETL in PbSe NR and PbSe QD based solar cells, Davis et.al<sup>3</sup> and Semonin et.al<sup>47</sup> were performed annealing under ambient conditions at 130°C for 5 minutes. As a first step for the optimization of ZnO ETL, annealing temperature was kept as 130°C and duration of the annealing process was tested. The solar cells with an architecture represented in Figure 4.8-a were fabricated to control the annealing process. Cells were annealed at 130°C for 5 min and 30 min. The cells were consisting of ZnO as ETL, 1 layer of EDT capped PbSe QD<sub>1.0 eV</sub> and 2 layers of EDT capped Bulk-1 as light absorbing active layer (blend of PbSe QD<sub>1.0 eV</sub> + SynP-NR<sub>0.95 eV</sub>), EDT capped PbSe QD<sub>1.4 eV</sub> as HTL and Ag metal as a back contact.

I-V and EQE/IQE spectra are shown in Figure 4.8 and cell performance parameters are summarized in Table 4.5. As represented in Figure 4.8-b, an increase was observed in a PCE from 0.14 to 0.26 when the annealing duration increased from 5 min to 30 min. EQE/IQE tests were performed to assess the origins of the current gain observed in I-V measurements. According to the EQE/IQE spectra represented in Figure 4.8-c, annealing duration has a significant role in the exciton generation in visible regions of the spectrum. EQE value at 500 nm increased from 28% to 48% with 30 min annealing duration.

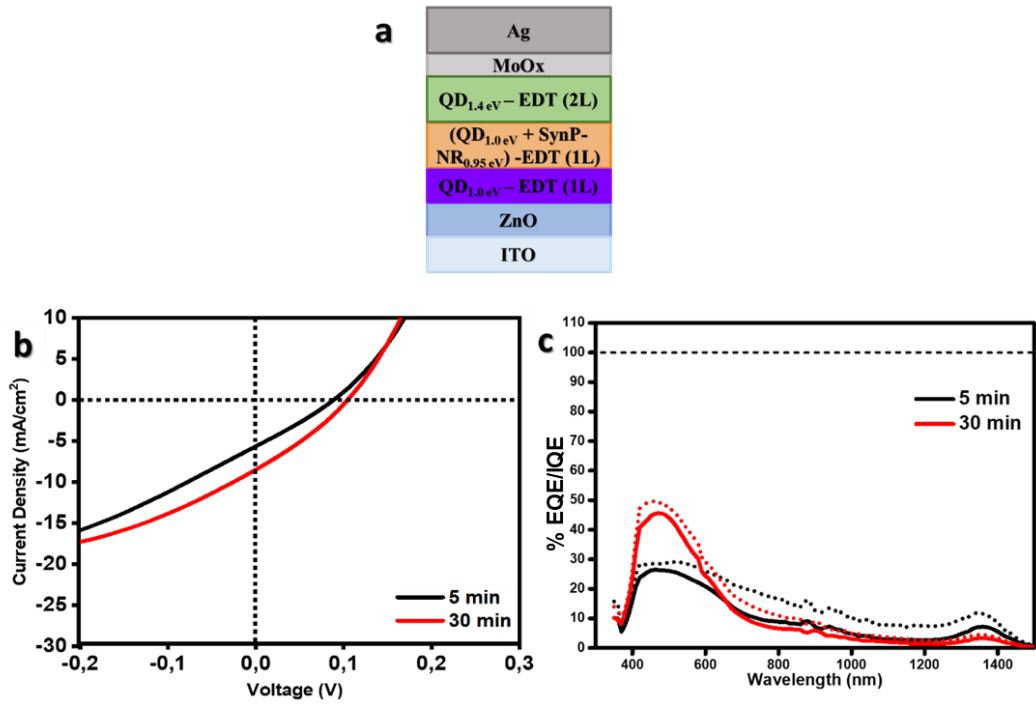


Figure 4.8. Role of the annealing duration of the ZnO layer on the photovoltaic performance of the solar cell. **a)** Cell architecture, **b)** I-V characteristics and **c)** EQE/IQE spectra.

Table 4.5 Effect of annealing duration of ZnO on solar cell characteristics.

<b>T</b> (°C)	<b>t</b> (min)	<b>Jsc</b> (mA.cm <sup>-2</sup> )	<b>Voc</b> (V)	<b>FF</b>	<b>PCE</b> (%)	<b>Jsc<sup>EQEa</sup></b> (mA.cm <sup>-2</sup> )	<b>Exp code</b>
130	5	5.72 ±0.26 (5.63)	0.09 ±0.01 (0.09)	25.86 ±0.18 (25.65)	0.14 ±0.01 (0.14)	5.70	BB_6_ c5_p8_ d1
130	30	8.12 ±0.40 (8.47)	0.11 ±0.00 (0.11)	26.71 ±1.96 (28.73)	0.23 ±0.02 (0.26)	6.32	BB_6_ c4_p4_ d4

<sup>a</sup> Theoretical J<sub>SC</sub> calculated from the EQE spectrum.

<sup>b</sup> Cell architecture: ITO / ZnO / PbSe QD<sub>1.0 eV</sub> -EDT (1L) / (Bulk) - EDT (1) / PbSe QD<sub>1.4 eV</sub> -EDT (2L) / MoOx / Ag where BULK: PbSe QD<sub>1.0 eV</sub> + SynP-PbSe NR<sub>0.95 eV</sub>

In the second step of the optimization of the ZnO ETL, cells containing ZnO with different dilution ratio and with different annealing temperatures were fabricated. The architecture of the cell is shown in the Figure 4.9-a. The cells were consisting of ZnO as ETL, 2 layers of EDT capped Bulk-1 as light absorbing active layer (blend of PbSe QD<sub>1.0 eV</sub> + SynP-NR<sub>0.97 eV</sub>), EDT capped PbSe QD<sub>1.4 eV</sub> as HTL and Au metal as a back contact.

As previously mentioned, transparency of the ZnO ETL plays an important role in cell performance. In this thesis, transparency studies were carried out by manipulating the dilution ratio of the DEZn in THF. As demonstrated in the Figure 4.9-b, the dilution ratio has a significant impact on the transparency of ETL. As the DEZn: THF dilution ratio changes from 1:4 to 1:5, the transmittance at 310 nm was increased from 55% to 65%. To acquire a deeper understanding of this topic and assess if this increase in transmittance leads to an enhancement in cell performance by allowing more light to reach the active layer, PbSe NRs and PbSe QDs-based BNHJ solar cells were fabricated. I-V and EQE/IQE spectra are shown in Figure 4.9 and cell performance parameters are summarized in Table 4.6. As represented in Figure 4.9-c, although a minor change in  $V_{oc}$  (from 0.41 V to 0.40 V) is noted, a dramatic decrease in  $J_{sc}$  (from 23.00 mA.cm<sup>-2</sup> to 18.81 mA.cm<sup>-2</sup>) was observed when the DEZn: THF dilution ratio changes from 1:4 to 1:5. EQE/IQE tests were performed to assess the origins of the current loss observed in I-V measurements. According to the EQE/IQE spectra represented in Figure 4.9-d, dilution ratio has a significant role in the exciton generation in all regions of the spectrum. Despite increasing the transparency at wavelengths less than 400 nm, ZnO ETLs prepared from 1:5 DEZn:THF volume ratio led to an insufficient carrier transport which we attribute to the inconvenient morphology of the ZnO.

In light of higher cell performances recorded for the ZnO layers annealed longer, further optimization was done for higher annealing temperatures. Annealing temperatures of 130°C and 150°C were tested on the cell architecture represented in

Figure 4.9-a and cell performance parameters are summarized in Figure 4.9. According to the transmittance measurements represented in Figure 4.9-b, similar %transmittance values were obtained for ZnO layers annealed at 130°C and 150°C for 30 min. According to the I-V characteristics represented in Figure 4.9-c, slight drop in cell performance (from 4.09% to 3.90%) was observed when annealing temperature of ZnO was increased from 130°C to 150°C. Increase in cell performance was mainly attributed to the slightly higher  $J_{sc}$  and FF values of ZnO annealed at lower temperature. EQE/IQE measurements were done to investigate the origins of the slight increase in  $J_{sc}$  from 20.35 to 21.34 when annealing temperature decreases from 150°C to 130°C. In accordance with the I-V characteristics, slightly higher EQE was recorded for wavelengths spanning ~550 nm to ~1100 nm (see Figure 4.9-d).

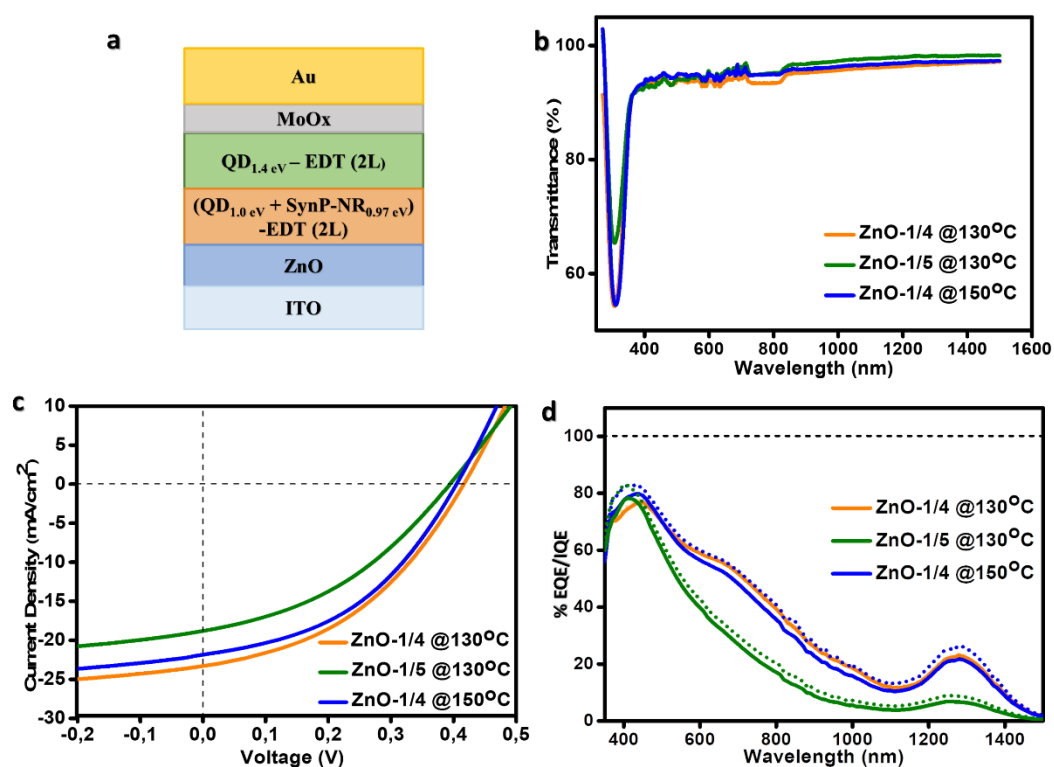


Figure 4.9. Role of the dilution ratio and the annealing temperature of the ZnO layer on the photovoltaic performance of the solar cell. **a)** Cell architecture, **b)** transmittance spectrum of ZnO thin films, **c)** I-V characteristics and **d)** EQE/IQE spectra.

Table 4.6 Effect of annealing temperature and dilution ratio of ZnO on solar cell characteristics.

<b>DEZ: THF</b>	<b>T (°C)</b>	<b>Jsc (mA.cm<sup>-2</sup>)</b>	<b>Voc (V)</b>	<b>FF</b>	<b>PCE (%)</b>	<b>Jsc<sup>EQEa</sup> (mA.cm<sup>-2</sup>)</b>	<b>Exp code</b>
1:4 <sup>b</sup>	130	21.54 ±1.10 (23.00)	0.41 ±0.01 (0.41)	42.54 ±0.90 (42.99)	3.73 ±0.31 (4.09)	21.34	IK_1 _c2_ p6_d 2
1:5 <sup>b</sup>	130	18.25 ±0.10 (18.81)	0.39 ±0.01 (0.40)	37.38 ±0.10 (37.74)	2.69 ±0.20 (2.84)	13.32	IK_1 _c9_ p2_d 5
1:4 <sup>b</sup>	150	20.45 ±0.61 (21.84)	0.41 ±0.11 (0.40)	41.86 ±2.30 (43.33)	3.60 ±0.10 (3.90)	20.35	IK_1 _c4_ p3_d 5

<sup>a</sup>Theoretical J<sub>SC</sub> calculated from the EQE spectrum.

<sup>b</sup> Cell architecture: ITO / ZnO / (Bulk)-EDT (2L) / PbSe QD<sub>1.4 eV</sub> -EDT (2L) / MoOx / Au where BULK: PbSe QD<sub>1.0 eV</sub> + SynP-PbSe NR<sub>0.97 eV</sub>

As a result, maximum PCE of 4.09% was achieved for cells prepared from optimized ETL where the ZnO layer was prepared from 1:4 DEZn: THF volume ratio and annealed at 130°C for 30 minutes.

#### 4.2.4 Effect of Active Layer Thickness on Cell Performance

Performance of the solar cells show a strong dependence on the thickness of the light absorbing active layer. With this purpose, the thickness of the BNHJ active layer was altered by increasing the number of L-B-L process from 2L to 6L. The architectures of the cells were shown in the Figure 4.10-a. The cells were consisting of ZnO as

ETL, 2-4-6 layers of light absorbing BNHJ blend (Bulk-1: PbSe QD<sub>1.0 eV</sub> + NR<sub>0.93 eV</sub>) as active layer, PbSe QD<sub>1.40 eV</sub> as HTL and Au as a back contact.

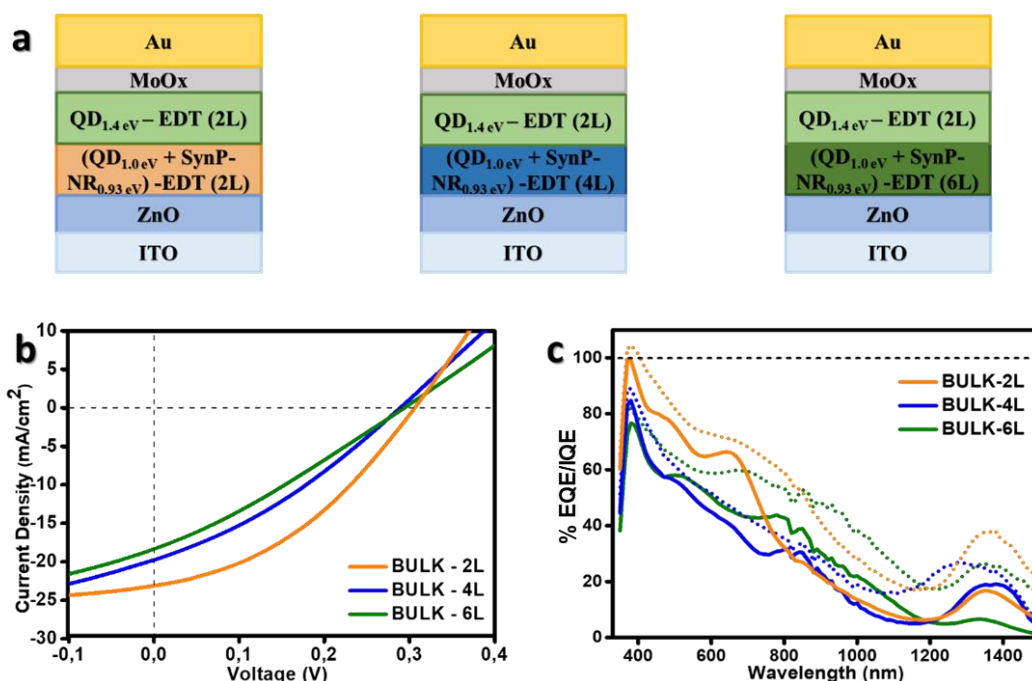


Figure 4.10. Role of the active layer thickness on the photovoltaic performance of the solar cell. **a)** Schematic representation of cell architectures, **b)** I-V characteristics and **c)** EQE/IQE spectra.

I-V characteristics of the cells are shown in Figure 4.10-b and performance parameters of the cells are summarized in Table 4.7. As the number of active layers increased, PCE of cells were affected drastically. According to Table 4.7, the major contribution to the decrease in PCE of the cells were assigned to the decrease in  $J_{sc}$ . In this sense,  $J_{sc}$  of the cell with 2 layers of active layer was measured as 23.11 mA.cm<sup>-2</sup>, while  $J_{sc}$  of cells with 4 and 6 layers of active layer yielded 19.77 mA.cm<sup>-2</sup> and 17.88 mA.cm<sup>-2</sup>, respectively. Maximum performance of 2.71% was obtained for the cells with 2 layers of active layer where  $V_{oc}$ , FF and  $J_{sc}$  were recorded as 0.307 V, 38.23% and 23.11 mA.cm<sup>-2</sup>, respectively. EQE tests were performed to investigate the origins of the photocurrent loss measured in I-V set up. As

represented in Table 4.7,  $J_{sc}$  values measured from I-V set-up were in agreement with the theoretical  $J_{sc}$  values calculated from the EQE set-up, which indicates the reliability of the two independent measurements. As represented in Figure 4.10-c, increase in active layer thickness led to a monotonic photocurrent loss in between 400 nm to 800 nm and wavelengths beyond 1200 nm. Maximum EQE was recorded as 100%, 85% and 77% at 380 nm for 2L, 4L and 6L, respectively. IQE, on the other hand, was measured as 105%, 89% and 82% for 2L, 4L and 6L, respectively. Generation of 105 photons per 100 photons absorbed at 380 nm indicates that the MEG mechanism is active in this cell architecture. As a result, we note that the active layer thickness plays a key role in creating multiple excitons; as the thickness of the light absorbing active layer decreases, photocurrent generation at wavelengths where MEG is expected to take place increases.

Table 4.7 Effect of active layer thickness on cell performance parameters.

# of Bulk Layer	Jsc (mA.cm <sup>-2</sup> )	Voc (V)	FF (%)	PCE (%)	Jsc <sup>EQEa</sup> (mA.cm <sup>-2</sup> )	Exp code
2L <sup>b</sup>	21.45 ±1.36 (23.11)	0.31± 0.00 (0.31)	36.75 ±2.01 (38.23)	2.57 ±0.20 (2.71)	21.25	IK_3_c 8 _p3_d5
4L <sup>b</sup>	17.40 ±2.60 (19.77)	0.28 ±0.07 (0.29)	28.05 ±2.04 (31.47)	1.79 ±0.10 (1.83)	18.74	IK_3_c 4 _p2_d1
6L <sup>b</sup>	18.36 ±2.40 (17.88)	0.28 ±0.07 (0.29)	27.85 ±1.93 (30.02)	1.45 ±0.30 (1.58)	16.10	IK_3_c 5 _p2_d1

<sup>a</sup> Theoretical J<sub>SC</sub> calculated from the EQE spectrum.

<sup>b</sup> Cell architecture: ITO / ZnO / (Bulk) - EDT (X) / PbSe QD<sub>1.4 eV</sub> -EDT (2L) / MoOx / Au where BULK: PbSe QD<sub>1.0 eV</sub> + SynP-PbSe NR<sub>0.93 eV</sub> and X: 2L, 4L and 6L.

#### 4.2.5 Optimization of the HTL

HTL is responsible for the extraction of holes in the active layer and transportation to the respective electrodes. This layer constructs an energy barrier to block electron transport to the anode and separates the active layer from the anode by lowering the likelihood of corrosion and degradation. This way the stability of cells was enhanced<sup>74</sup>. High-performance solar cells require the development of efficient hole transport layers. Better charge collection by correctly optimized energy level alignment between the active layer and hole transport material is crucial for the enhancement of the solar cell performance. HTLs can be in a variety of forms, including inorganic, polymeric, and organic molecules<sup>75</sup>. In light of these

information, three different HTL layers were tested and the changes in cell parameters were examined. PbSe QDs (1.4 eV), TIPS-Pentacene molecule and PbS QDs (1.3 eV) were used as HTLs for this study. The architecture of the cells was shown in the Figure 4.11-a. The cells were consisting of ZnO as ETL, two layers of EDT capped BNHJ blend (Bulk-1: PbSe QD<sub>1.0 eV</sub> + SynP-NR<sub>0.95 eV</sub>) and Au as a back contact.

Absorbance measurements of the light absorbing active layer (Bulk-1) and its components (PbSe QD (1.0 eV) and SynP-PbSe NR (0.95 eV)) are shown in Figure 4.11-b. The absorbance spectrum of the blend is the sum of the absorbances of the individual components. Additionally, Figure 4.11-c represents the absorbance spectrum of the HTLs. Unique peaks of TIPS-Pentacene in the range between 500nm -650 nm were observed in the absorbance spectrum.

UPS measurements were conducted to determine the energy alignment of the cell components. According to the energy landscape of cell components represented in Figure 4.11-d, HTLs utilized in this thesis study effectively allow for the extraction of holes. Conduction band level of TIPS-Pentacene was measured as -3.1 eV. This creates a barrier of around 0.8 eV to electrons originating from the nanorod and 1.1eV to electrons originating from QDs in the bulk and can prevent electrons from moving in the opposite direction. Additionally, when the conduction/valence band levels of the PbS QD layer were compared with Bulk-1 and its cell components, it is seen that hole conduction is possible from both the quantum dot and the nanorod.

I-V characteristics of the cells are shown in the Figure 4.11-e and performance parameters of the cells are summarized in the Table 4.8. Record PCE of 2.62% was measured for the cells where PbSe QD<sub>1.4 eV</sub> was used as HTL. Cell performance of PbS QDs (2.56% PCE) was similar to the cells where PbSe QDs were used as HTL. When the I-V parameters summarized in Table 4.8 are examined, it is seen that the FF value is greatly reduced in cells in which the TIPS- Pentacene molecule was used as HTL.

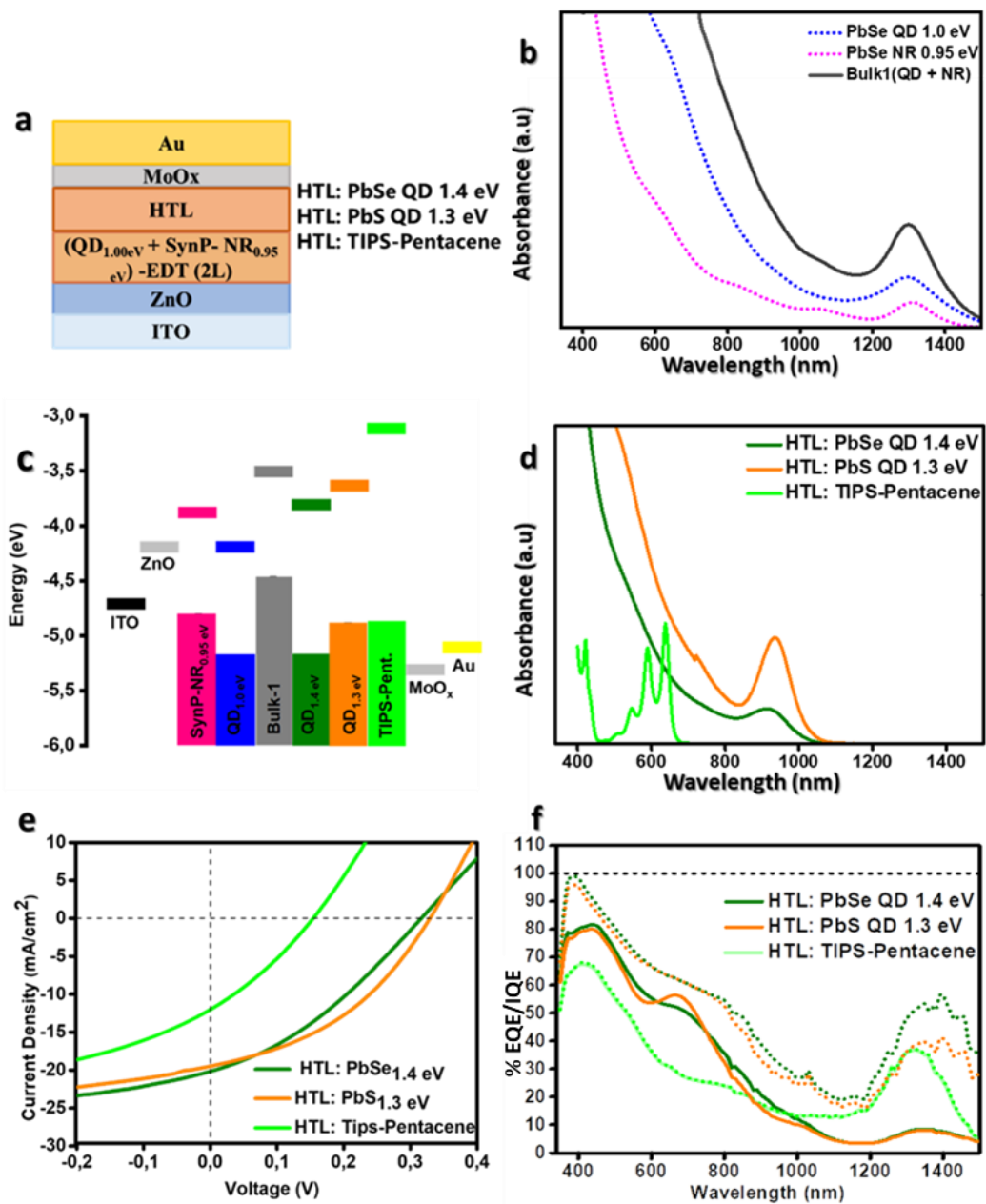


Figure 4.11. Role of the HTL on the photovoltaic performance of the solar cell. **a**) Schematic representation of the cell architecture, **b**) absorbance spectra of EDT capped light absorbing active layer (Bulk-1) and its components; EDT capped SynP-PbSe NR<sub>0.95 eV</sub> and EDT capped PbSe QD<sub>1.0 eV</sub>, **c**) energy landscape of cell components determined from UPS, **d**) absorbance spectra of TIPS-Pentacene, EDT capped PbSe QD<sub>1.4 eV</sub> and EDT capped PbS QD<sub>1.3 eV</sub> as HTLs, **e**) I-V characteristics and **f**) EQE/IQE spectra.

The source of the dramatic decrease in  $J_{sc}$  for cells where TIPS-Pentacene was used as HTL was examined by the EQE measurements. According to the results shown in Figure 4.11-f, EQE value at 1300 nm increased from 10% to 40% with TIPS-Pentacene HTL. This 4-fold increase in the EQE at wavelengths where the photocurrent generation is due to the excitons generated by Bulk-1 was assigned to the effective transfer of holes from Bulk-1 to TIPS-Pentacene molecule. On the other hand, a sharp decrease in EQE observed between 350 nm and 800 nm was attributed to be the undesired downstream diffusion of the TIPS-Pentacene molecule during the spin coating process. As a result of this diffusion, it was concluded that the TIPS-Pentacene molecules were penetrated into the heterojunction layer and absorbed most of the high-energy photons entering to the cell. This leads to a drastic decrease in the exciton formation in the front of the cell where MEG is expected to take place.

Table 4.8 Effect of the HTL on the cell performance parameters.

HTL <sup>a</sup>	$J_{sc}$ (mA.cm <sup>-2</sup> )	Voc (V)	FF (%)	PCE (%)	$J_{sc}^{EQEb}$ (mA.cm <sup>-2</sup> )	Exp code
PbSe QD <sub>1.4 eV</sub>	18.56 ± 0.06 (18.42)	0.34 ± 0.01 (0.35)	38.62 ± 1.16 (41.05)	2.40 ± 0.09 (2.62)	20.17	IK_2_c 1_p3_d 2
TIPS- Pentacene	13.76 ± 1.10 (13.64)	0.20 ± 0.11 (0.21)	32.72 ± 1.04 (32.77)	0.90 ± 0.09 (0.95)	15.66	IK_2_c 3_p1_d 3
PbS QD <sub>1.3 eV</sub>	18.15 ± 0.67 (19.50)	0.33 ± 0.00 (0.33)	36.73 ± 2.06 (39.30)	2.27 ± 0.03 (2.56)	18.55	IK_2_c 5_p3_d 3

<sup>a</sup> Cell architecture: ITO / ZnO / (Bulk)-EDT (2 L) / HTL / MoOx / Au where BULK: PbSe QD<sub>1.0 eV</sub> + SynP-PbSe NR<sub>0.95 eV</sub> and HTL: PbSe QD<sub>1.4 eV</sub> -EDT (2L), TIPS-Pentacene and PbS QD<sub>1.3 eV</sub> -EDT(2L).

<sup>b</sup> Theoretical  $J_{sc}$  calculated from the EQE spectrum.

When the performance parameters of cells with PbS QD<sub>1.3 eV</sub> HTL were examined, a slight increase in J<sub>SC</sub> value from 18.42 to 19.50 was noted for PbS QD<sub>1.3 eV</sub> HTL. However, the cell efficiency did not show a significant change. When the IQE spectra were compared to PbSe QD<sub>1.4 eV</sub> HTL, PbS QD<sub>1.3 eV</sub> HTL led to an IQE value reaching 40% in the area where the nanorods absorb light. This is a proof that it contributes to hole conduction in the prescribed manner.

#### 4.2.6 Effect of Ligand Structure

As synthesized NRs and QDs are surrounded by the insulating oleate chains as a result of their synthesis. In order for those NPs to be utilized in photovoltaic applications, OA-capped NPs must be treated with relatively shorter surface ligands. The selection of a surface ligand has a significant impact on the degree of ordering of NRs and photovoltaic performance of a solar cell<sup>80</sup>. In this sense, 1,2-ethanedithiol (EDT) and 1,4-benzenedithiol (BDT) are the most widely used surface ligands in the literature to investigate the effect of surface ligands on degree of ordering and photovoltaic performance of QDs<sup>76-78</sup>. In light of these information, BNHJ blends prepared by blending QDs with NRs were treated with EDT and BDT and the impact of the surface ligand structure on cell performance was investigated.

Absorbance spectrum of the OA capped, EDT and BDT exchanged films is represented in Figure 4.12-a. As shown in absorbance spectrum excitonic peaks were red shifted in both BDT and EDT exchanged thin films due to electron coupling between NRs. But ligand structure does not affect the absorption characteristics significantly.

To explore the impacts of structure of ligand on the thin film morphology, TEM images (as seen in Figure 4.12-b,c) of EDT and BDT exchanged PbSe NRs were analyzed. EDT exchanged NRs are lined up in a more organized way whereas BDT exchanged NRs shows disordered thin films, which may have negative consequences on the exciton formation and transport.

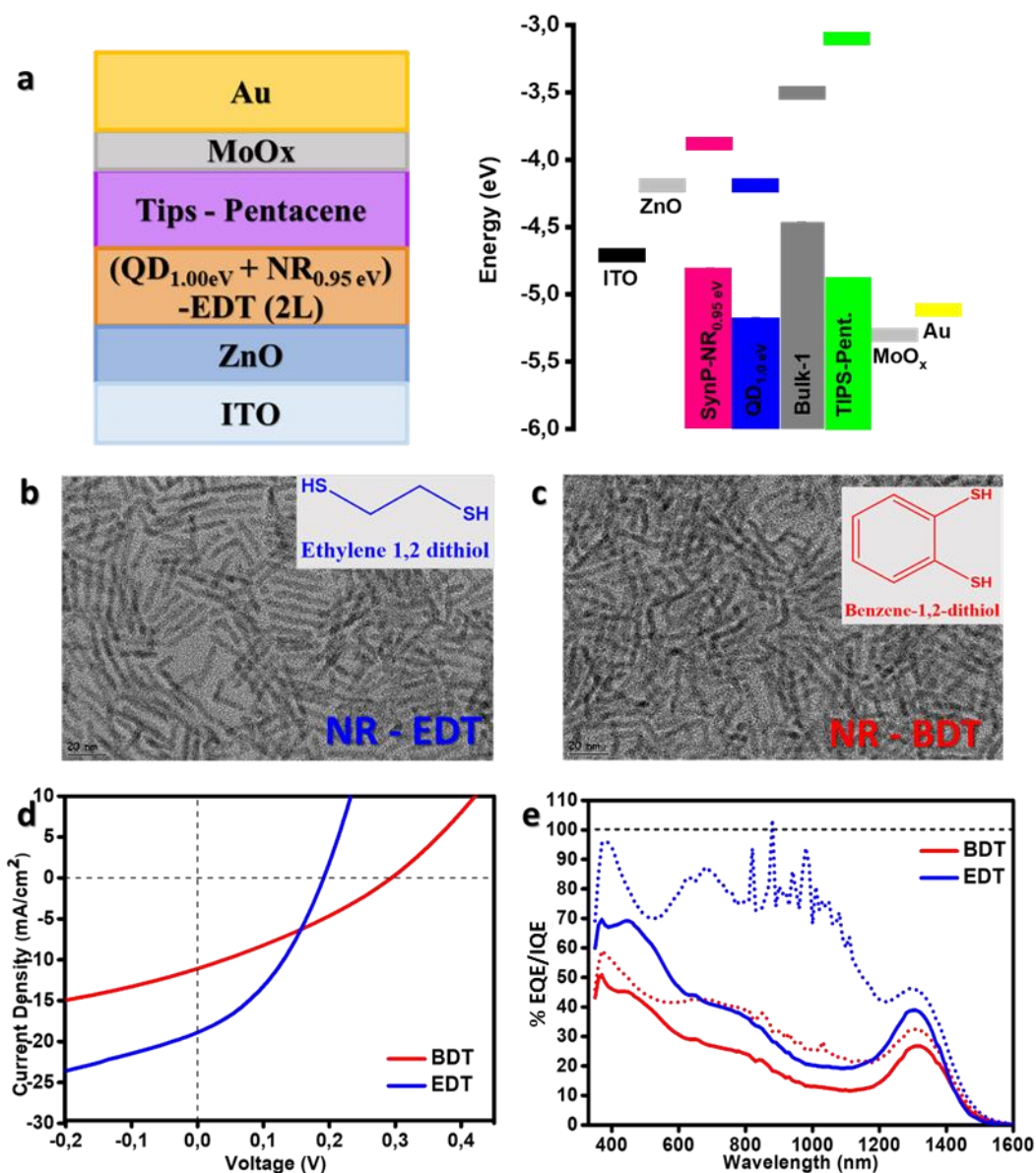


Figure 4.12. Role of the ligand structure on the photovoltaic performance of the solar cell. **a)** Cell architecture and energy landscape of the cell components, **b)** TEM image of and BDT exchanged NRs thin film, **c)** TEM images of EDT exchanged NRs thin film, **d)** I-V characteristics and **e)** EQE/IQE spectra.

To investigate the effect of ligand structure on the photovoltaic performance of the cells, EDT and BDT ligand exchanged cells were fabricated. As represented in Figure 4.12-a, the cells were consisting of ZnO as ETL, two layers of Bulk-1 (PbSe QD<sub>1.0eV</sub> + NR<sub>0.95eV</sub>) as the light absorbing active layer and TIPS-Pentacene as HTL.

According to the energy landscape represented in Figure 4.12-a, QDs and NRs act as acceptor and donor units, respectively and TIPS-Pentacene act as an effective HTL.

I-V characteristics of the cells were shown in the Figure 4.12-d and performance parameters of the cells were summarized in the Table 4.9. The cell with EDT as ligand showed better performance,  $V_{OC}$  was 0.187 V, the FF was 38.24 PCE was 1.350 and  $J_{SC}$  was  $18.89 \text{ mA}\cdot\text{cm}^{-2}$  that in agreement with the  $J_{SC}$  from the QE measurement. Comparing cells revealed that EDT exchanged cell yielded the highest current, while BDT exchanged cell yielded the highest  $V_{OC}$ . Although the  $V_{OC}$  (0.293 V) of the cell with BDT ligand was higher than the  $V_{OC}$  of the EDT exchanged cell, other parameters showed dramatically drop.

In addition to a severe decrease in cell characteristics, the QE in the whole spectrum also decreased when BDT was utilized as the ligand as seen in Figure 4.12-e. The decrease in the cell performance can be attributed to the disordered thin film formation with the BDT ligand. The peaks in IQE around 600-800 nm were belong to TIPS-Pentacene molecules.

I-V characteristics of the cells are shown in the Figure 4.12-d and performance parameters of the cells are summarized in the Table 4.9. The cell where Bulk-1 was ligand exchanged with EDT showed better performance as compared to cells where BDT was used as the surface ligand. Higher PCE of the EDT treated BNHJ layers was assigned mainly to the increase in  $J_{SC}$  and FF values.

In order to examine the origins of the severe photocurrent loss for the BDT ligand, EQE/IQE measurements were performed on solar cells. According to the EQE/IQE spectra represented in Figure 4.12-e, the sharp drop in  $J_{SC}$  is due to the drop in exciton generation at all wavelengths between 340 nm to 1500 nm. In addition to the peak at 1300 nm, which was attributed to the excitons generated in the Bulk-1, additional peaks were observed at 630 and 690 nm. These were assigned to the TIPS-Pentacene molecules which shows that TIPS-Pentacene molecules not only act as HTL but also contributes to the photocurrent when EDT is used as the ligand to bind NRs donor

to QD acceptor. Additionally, the IQE goes beyond %100 at 880 nm for solar cells where EDT was used to exchange the surface ligands of Bulk-1. This was attributed to the MEG process.

Table 4.9 Effect of ligand structure on the cell performance parameters.

<b>Ligand Type</b>	<b>Jsc (mA.cm<sup>-2</sup>)</b>	<b>Voc (V)</b>	<b>FF</b>	<b>PCE (%)</b>	<b>Jsc<sup>EQEa</sup> (mA.cm<sup>-2</sup>)</b>	<b>Exp code</b>
BDT <sup>b</sup>	9.71 ±1.15 (11.09)	0.29 ±0.06 (0.29)	30.98 ±2.72 (30.39)	0.86 ±0.08 (0.99)	13.26	IK_6_c4 _p4_d3
EDT <sup>b</sup>	18.2 0±0.68 (18.89)	0.17 ±0.02 (0.19)	35.01 ±2.25 (38.24)	1.07 ±0.22 (1.35)	20.28	IK_6_c5 _p2_d1

<sup>a</sup>Theoretical J<sub>SC</sub> calculated from the EQE spectrum.

<sup>b</sup>Cell architecture: ITO / ZnO / Bulk-X (2 L) / TIPS-Pentacene / MoOx / Au where BULK: PbSe QD<sub>1.0 eV</sub> + PbSe NR<sub>0.95 eV</sub> and X: EDT or BDT.

## CHAPTER 5

### CONCLUSION

In this thesis, strategies to enhance the cell performance of MEG based PbSe QD/NR solar cells are suggested. High quality QDs and NRs with high monodispersity values were synthesized with hot injection method. Several parameters such as the cell components (ETL, HTL, front layer), annealing duration and temperature of the ZnO ETL and type of the ligand which interconnects QDs and NRs were optimized throughout this thesis. ZnO ETL was prepared by dilution of DEZn in THF. It was determined that the increase in dilution ratio and annealing temperature decreases the cell performance whereas increasing the duration of the annealing from 5 minutes to 30 minutes doubles the cell performance. The highest efficiency (4.09%) was achieved for the PbSe NR/QD based BNHJ solar cells with a dilution ratio of 1/4 and annealing at 130°C for 30 min.

PbSe QD/NR BNHJ platform was further optimized by removing the previously reported QD front layer. The resulting cell structure led to an enhancement in photocurrent generation in regions where MEG is expected to take place and enhanced the PCE from  $0.79 \pm 0.01\%$  to  $1.97 \pm 0.02\%$ .

On the other hand, increasing the thickness of the light absorbing bulk layer dramatically reduced the cell performance (from 2.71% for 2L to 1.58% for 6L) which was mainly attributed to a significant drop in  $J_{sc}$  (from  $23.11 \text{ mA}\cdot\text{cm}^{-2}$  for 2L to  $17.88 \text{ mA}\cdot\text{cm}^{-2}$  for 6L). We also note that the active layer thickness plays a key role in creating multiple excitons; as the thickness of the light absorbing active layer decreases, photocurrent generation at wavelengths where MEG is expected to take place increases. An increase of IQE at 380 nm from 82 to 105 as the number of active layer decreases from 6L to 2L points out to the essential role of active layer thickness on the MEG mechanism. In addition to the thickness, annealing of the active layer

(at 70°C for 5 min inside the GB before HTL coating) increased the cell performance from 0.53% to 0.86%. This enhancement was mainly attributed to the dramatic increase in  $J_{sc}$ . The effect of HTL on cell performance was investigated by utilizing PbSe QDs with 1.4 eV band gap, PbS QDs with 1.3 eV band gap and TIPS-Pentacene molecule. Champion cell was obtained with HTL where PbSe QDs with 1.4 eV band gap were used. Furthermore, the effect of ligand structure on cell performance was examined by performing the ligand exchange process with two different ligands; EDT and BDT. Cells with EDT showed higher performance as a result of higher degree of packing order in EDT exchanged NRs. Additionally, IQE of the cells, where EDT surrounded BNHJ layer were used as the active layer, goes beyond 100% (104%) at 880 nm which is the lowest MEG threshold energy reported up to date.

Based on the strategies summarized above, the resulting optimized BNHJ cells led to the cells with highest performance in the literature; over 100% EQE and 105% IQE and 4.09% PCE.

The ultimate aim of this thesis was to investigate the donor-acceptor properties of PbSe QDs and NRs by altering the respective donor and acceptor roles of NPs in optimized cell structures. In this sense, this thesis study reveals the key parameters playing crucial roles in improving the cell performance and MEG efficiency for the cells where NRs and QDs act as donor and acceptor unit. Further solar cells, where Bulk-2 (CB energy of NRs and QDs are balanced so no bulk nano-heterojunction is formed) and Bulk-3 (Donor: 1.85 eV PbSe QDs and Acceptor: 0.95 eV PbSe NRs) layers are utilized as light absorbing layer, will be fabricated in near future. Furthermore, spectroscopic studies such as photoluminescence and carrier lifetime will be carried out on respective thin films to reveal the carrier dynamics in near future.

## REFERENCES

1. Shockley W, Queisser HJ. Detailed balance limit of efficiency of p-n junction solar cells. *J. Appl. Phys.* 1961;32(3):510-519. doi:10.1063/1.1736034
2. Asil D, Walker BJ, Ehrler B, et al. Role of PbSe Structural Stabilization in Photovoltaic Cells. *Adv. Funct. Mater.* 2015;25(6):928-935. doi:10.1002/adfm.201401816
3. Davis NJLK, Böhm ML, Tabachnyk M, et al. Multiple-Exciton Generation in Lead Selenide Nanorod Solar Cells with External Quantum Efficiencies Exceeding 120%. *Nat. Commun.* 2015;6(1):1-7. doi:10.1038/ncomms9259
4. Konstantatos G, Sargent EH. *Colloidal Quantum Dot Optoelectronics and Photovoltaics*. Cambridge University Press; 2013.
5. Rogach AL, Gaponik N, Lupton JM, et al. Light-emitting diodes with semiconductor nanocrystals. *Angew. Chem. Int. Ed.* 2008;47(35):6538-6549. doi:10.1002/anie.200705109
6. Aydt AP, Blair S, Zhang H, Chernomordik BD, Beard MC, Berezin MY. Synthesis and spectroscopic evaluation of PbS quantum dots emitting at 1300 nm for optimized imaging in optical window II. *Reporters, Markers, Dyes, Nanoparticles, and Molecular Probes for Biomedical Applications VIII*. 2016;9723:72-81. doi:10.1117/12.2214509
7. Eisler HJ, Sundar VC, Bawendi MG, Walsh M, Smith HI, Klimov V. Color-selective semiconductor nanocrystal laser. *Appl. Phys. Lett.* 2002;80(24):4614-4616. doi:10.1063/1.1485125
8. García De Arquer FP, Gong X, Sabatini RP, et al. Field-emission from quantum-dot-in-perovskite solids. *Nat. Commun.* 2017;8(1):1-8. doi:10.1038/ncomms14757

9. Ganesan AA, Houtepen AJ, Crisp RW. Quantum dot solar cells: Small beginnings have large impacts. *Appl. Sci.* 2018;8(10):1867. doi:10.3390/app8101867
10. Shrestha A, Batmunkh M, Tricoli A, Qiao SZ, Dai S. Near-Infrared Active Lead Chalcogenide Quantum Dots: Preparation, Post-Synthesis Ligand Exchange, and Applications in Solar Cells. *Angew. Chem. Int. Ed.* 2019; 58(16):5202-5224. doi:10.1002/anie.201804053
11. Ma W, Luther JM, Zheng H, Wu Y, Alivisatos AP. Photovoltaic devices employing ternary PbS xSe 1-x nanocrystals. *Nano Lett.* 2009;9(4):1699-1703. doi:10.1021/nl900388a
12. Lipovskii A, Kolobkova E, Petrikov V, et al. Synthesis and characterization of PbSe quantum dots in phosphate glass. *Appl. Phys. Lett.* 1997;71(23): 3406-3408. doi:10.1063/1.120349
13. Sahoo, S. K. (2022). Sensing and biosensing with optically active nanomaterials: a note. In *Sensing and Biosensing with Optically Active Nanomaterials* (pp. 1-7). Elsevier15. Klimov VI. Spectral and dynamical properties of multiexcitons in semiconductor nanocrystals. *Annu. Rev. Phys. Chem.* 2007;58:635-673. doi:10.1146/annurev.physchem. 58.032806.104537
16. Tisdale WA, Zhu XY. Artificial atoms on semiconductor surfaces. *Proc. Natl. Acad. Sci. USA.* 2011;108(3):965-970. doi:10.1073/pnas.1006665107
17. Chukwuocha EO, Onyeaju MC, Harry TST. Theoretical Studies on the Effect of Confinement on Quantum Dots Using the Brus Equation. *World J. Condens. Matter Phys.* 2012;02(02):96-100. doi:10.4236/wjcmp.2012.22017
18. Abdulkareem Ghassan A, Mijan NA, Hin Taufiq-Yap Y. Nanomaterials: An Overview of Nanorods Synthesis and Optimization. In: *Nanorods and Nanocomposites*. IntechOpen; 2020. doi:10.5772/intechopen.84550

19. Huynh WU, Alivisatos AP, Peng X. CdSe Nanocrystal Rods/Poly(3-hexylthiophene) Composite Photovoltaic Devices. *Adv. Mater.* 1999;11(11):923-927. doi: [https://doi.org/10.1002/\(SICI\)1521-4095\(199908\)11:11<923::AID-ADMA923>3.0.CO;2-T](https://doi.org/10.1002/(SICI)1521-4095(199908)11:11<923::AID-ADMA923>3.0.CO;2-T)
20. Liu H, Zhong H, Zheng F, et al. Near-Infrared Lead Chalcogenide Quantum Dots: Synthesis and Applications in Light Emitting Diodes \*. *Chin. Phys.* 2019;28(12):128504.
21. Kagan CR, Murray CB. Charge transport in strongly coupled quantum dot solids. *Nat. Nanotechnol.* 2015;10(12):1013-1026. doi:10.1038/nnano.2015.247
22. Murray CB, Kagan CR, Bawendi MG. Synthesis and Characterization of Monodisperse Nanocrystals and Close-Packed Nanocrystal Assemblies. *Annu. Rev. Mater. Sci.* 2000;30(1):545-610. [www.annualreviews.org](http://www.annualreviews.org)
23. Lamer VK, Dinegar RH. Theory, Production and Mechanism of Formation of Monodispersed Hydrosols. *J. Am. Chem. Soc.* 1950;72(11):4847-4854.
24. Agrawal A, Cho SH, Zandi O, Ghosh S, Johns RW, Milliron DJ. Localized Surface Plasmon Resonance in Semiconductor Nanocrystals. *Chem. Rev.* 2018;118(6):3121-3207. doi: 10.1021/acs.chemrev.7b00613
25. Lifshitz IM, Slyozov V v. The Kinetics of Precipitation from Supersaturated Solid Solutions. *J. Phys. Chem. Solids.* 1961;19(2):35-50.
26. Wagner C, Wagner C. Theorie der Alterung von Niederschliigen durch Umlosen (Ostwald-Reifung). *Zeitschrift für Elektrochemie, Berichte der Bunsengesellschaft für physikalische Chemie.* 1961;65(7-8):581-591.
27. Talapin D v., Lee JS, Kovalenko M v., Shevchenko E v. Prospects of colloidal nanocrystals for electronic and optoelectronic applications. *Chem. Rev.* 2010;110(1):389-458. doi:10.1021/cr900137k

28. Hacıfendioglu T, Asil D. PbSe Nanorods for Hybrid Solar Cells: Optimization of Synthesis Protocols and Investigation of Surface Stability. In: *International Conference on Photovoltaic Science and Technologies (PVCon)*. IEEE; 2018:1-5. doi:10.1109/PVCon.2018.8523936
29. Yin Y, Alivisatos A. Colloidal nanocrystal synthesis and theorganic–inorganic interface. *Nature*. 2005;437(7059):664-670.
30. Wu Z, Yang S, Wu W. Shape control of inorganic nanoparticles from solution. *Nanoscale*. 2016;8(3):1237-1259. doi:10.1039/c5nr07681a
31. Hacıfendioglu T., Asil D. Aspect Ratio Dependent Air Stability of PbSe Nanorods and Photovoltaic Applications. *Turk. J. of Chem*. 2021;45(3):905-913. doi:10.3906/kim-2012-6
32. Hersch P, Zweibel K, Energy Research Institute S. *Basic Photovoltaic Principles and Methods.*; 1982.
33. Riordan C, Hulstrom R. What Is an Air Mass 1.5 Spectrum? In: *Conference on Photovoltaic Specialists.*; 1990:1085-1088.
34. Würfel P, Würfel U. *Physics of Solar Cells.*; 2003.
35. Standard Solar Spectra | PVEducation. Accessed June 23, 2022. <https://www.pveducation.org/pvcdrom/appendices/standard-solar-spectra>
36. Hersch P, Zweibel K. *Basic Photovoltaic Principles and Methods.*; 1982.
37. Markvart T, Castañer L. Principles of Solar Cell Operation. In: *Solar Cells*. Elsevier Ltd; 2013:3-25. doi:10.1016/B978-0-12-386964-7.00001-9
38. Markvart T, Castañer L. Principles of Solar Cell Operation. In: *Solar Cells*. Elsevier Ltd; 2013:3-25. doi:10.1016/B978-0-12-386964-7.00001-9
39. External Quantum Efficiency Measurement of Solar Cell. In: *15th International Conference on Quality in Research (QiR): International Symposium on Electrical and Computer Engineering*. IEEE; 2017:450-456.

40. Fraas L, Partain L. *Solar Cells and Their Applications, 2nd Edition (Wiley Series in Microwave and Optical Engineering)*.; 2010.
41. Best Research-Cell Efficiencies. Accessed June 23, 2022. <https://www.nrel.gov/pv/assets/pdfs/best-research-cell-efficiencies-rev220126b.pdf>
42. Pandikumar A, Ramaraj R. *Rational Design of Solar Cells for Efficient Solar Energy Conversion*.; 2018.
43. Kumar, Pankaj. *Organic Solar Cells. Device Physics, Processing, Degradation, and Prevention*.; 2016.
44. Polman A, Knight M, Garnett EC, Ehrler B, Sinke WC. Photovoltaic materials: Present efficiencies and future challenges. *Science (1979)*. 2016;352(6283):4424. doi:10.1126/science.aad4424
45. Nozik AJ. Multiple exciton generation in semiconductor quantum dots. *Chem. Phys. Lett.* 2008;457(1-3):3-11. doi: 10.1016/j.cplett. 2008.03.094
46. Böhm ML, Jellicoe TC, Tabachnyk M, et al. Lead telluride quantum dot solar cells displaying external quantum efficiencies exceeding 120%. *Nano Lett.* 2015;15(12):7987-7993. doi: 10.1021/acs.nanolett.5b03161
47. Semonin OE, Luther JM, Choi S, et al. Peak External Photocurrent Quantum Efficiency Exceeding 100% via MEG in a Quantum Dot Solar Cell. *Science (1979)*. 2011;334(6062):1530-1533. <http://science.sciencemag.org/>
48. Hacıfendioğlu T. *Development of Solar Cells Based on Surface Passivated Lead Telluride Quantum Dots and Lead Selenide Nanorods; a Comprehensive Approach Targeting the Instability and Surface Mediated Trap States*. 2020.
49. Padilha LA, Stewart JT, Sandberg RL, et al. Carrier multiplication in semiconductor nanocrystals: Influence of size, shape, and composition. *Acc. Chem. Res.* 2013;46(6):1261-1269. doi:10.1021 /ar300228x

50. Ma W, Swisher SL, Ewers T, et al. Photovoltaic performance of ultrasmall PbSe quantum dots. *ACS Nano*. 2011;5(10):8140-8147. doi:10.1021/nl202786g
51. Konstantatos G, Sargent EH. *Colloidal Quantum Dot Optoelectronics and Photovoltaics*. Cambridge University Press; 2013.
52. Luther JM, Law M, Beard MC, et al. Schottky solar cells based on colloidal nanocrystal films. *Nano Lett*. 2008;8(10):3488-3492. doi:10.1021/nl802476m
53. Ahmad W, He J, Liu Z, et al. Lead Selenide (PbSe) Colloidal Quantum Dot Solar Cells with >10% Efficiency. *Adv. Mater.* 2019;31(33):1900593. doi:10.1002/adma.201900593
54. Han L, Liu J, Yu N, et al. Facile synthesis of ultra-small PbSe nanorods for photovoltaic application. *Nanoscale*. 2015;7(6):2461-2470. doi:10.1039/c4nr05707d
55. Gur I, Fromer NA, Geier ML, Alivisatos AP. Air-Stable All-Inorganic Nanocrystal Solar Cells Processed from Solution. *Science (1979)*. 2005;310(5747):462-465.
56. Koh WK, Bartnik AC, Wise FW, Murray CB. Synthesis of Monodisperse PbSe Nanorods: A case for oriented attachment. *J. Am. Chem. Soc.* 2010; 132(11):3909-3913. doi:10.1021/ja9105682
57. Hou B, Cho Y, Kim BS, et al. Highly Monodispersed PbS Quantum Dots for Outstanding Cascaded-Junction Solar Cells. *ACS Energy Letters*. 2016; 1(4):834-839. doi:10.1021/acsenerylett.6b00294
58. Barkhouse DAR, Debnath R, Kramer IJ, et al. Depleted bulk heterojunction colloidal quantum dot photovoltaics. *Adv. Mater.* 2011;23(28):3134-3138. doi:10.1002/adma.201101065

59. Carlson B, Leschkies K, Aydil ES, Zhu XY. Valence band alignment at cadmium selenide quantum dot and zinc oxide (10 $\bar{1}$ 0) interfaces. *J. Phys. Chem. C*. 2008;112(22):8419-8423. doi:10.1021/jp7113434
60. Hacıfendioglu T, Asil D. PbSe Nanorods for Hybrid Solar Cells: Optimization of Synthesis Protocols and Investigation of Surface Stability. In: *International Conference on Photovoltaic Science and Technologies (PVCon)*. IEEE; 2018.
61. Semonin OE, Luther JM, Beard MC. Quantum dots for next-generation photovoltaics. *Materials Today*. 2012;15(11):508-515.
62. Kim S, Marshall AR, Kroupa DM, et al. Air Stable and Efficient PbSe Quantum Dot Solar Cells Based upon ZnSe to PbSe Cation-Exchanged Quantum Dots.
63. Cheng F, Yu M, Jia L, et al. Ultra-small PbSe Quantum Dots Synthesis by Chemical Nucleation Controlling. *J. Wuhan Univ. Technol. Mater. Sci. Ed.* 2021;36(4):478-483. doi:10.1007/s11595-021-2433-7
64. Ehrler B, Walker BJ, Böhm ML, et al. In situ measurement of exciton energy in hybrid singlet-fission solar cells. *Nat. Commun.* 2012; 3:1019. doi:10.1038/ncomms2012
65. Yang L, Tabachnyk M, Bayliss SL, et al. Solution-processable singlet fission photovoltaic devices. *Nano Letters*. 2015;15(1):354-358. doi:10.1021/nl503650a
66. Du K, Liu G, San H, Chen X, Wang K. PbS Quantum Dots and Au Nanoparticle Co-Sensitized Black TiO<sub>2</sub> Nanotubes for Photocurrent Enhancement. *ECS Transactions*. 2016;75(1):125-134. doi:10.1149/07501.0125ecst
67. Dai L, Zhi C. *Flexible Energy Conversion and Storage Devices*. John Wiley & Sons; 2018.

68. Chen LC, Tseng ZL. ZnO-Based Electron Transporting Layer for Perovskite Solar Cells. In: *Nanostructured Solar Cells*. InTech; 2017:203-215. doi:10.5772/65056
69. Gyawali S, Goni LKMO, Chowdhury MS, et al. Effect of KOH concentration on the properties of ZnO nanoparticles. *Mater. Res. Express*. 2022;9(5). doi:10.1088/2053-1591/ac6b8a
70. Goodwin H, Jellicoe TC, Davis NJLK, Böhm ML. Multiple exciton generation in quantum dot-based solar cells. *Nanophotonics*. 2018;7(1):111-126. doi:10.1515/nanoph-2017-0034
71. Takahashi A, Wang H, Fukuda T, Kamata N, Kubo T, Segawa H. Annealing-temperature dependent carrier-transportation in ZnO/PbS quantum dot solar cells fabricated using liquid-phase ligand exchange methods. *Energies (Basel)*. 2020;13(19):5037. doi:10.3390/en13195037
72. Sanchez JG, Torimtubun AAA, Balderrama VS, Estrada M, Pallares J, Marsal LF. Effects of Annealing Temperature on the Performance of Organic Solar Cells Based on Polymer: Non-Fullerene Using V2O5 as HTL. *IEEE J. of the Electron Devices Soc*. 2020;8:421-428. doi:10.1109/JEDS.2020.2964634
73. Yi Z, Ni W, Zhang Q, et al. Effect of thermal annealing on active layer morphology and performance for small molecule bulk heterojunction organic solar cells. *J. of Mater. Chem. C*. 2014;2(35):7247-7255. doi:10.1039/c4tc00994k
74. Li S, Cao YL, Li WH, Bo ZS. A brief review of hole transporting materials commonly used in perovskite solar cells. *Rare Metals*. 2021;40(10):2712-2729. doi:10.1007/s12598-020-01691-z
75. Hosseini S, Delibaş N, Bahramgour M, Tabatabaei Mashayekh A, Niaie A. Performance Comparison of Different Hole Transport Layer Configurations in a Perovskite-based Solar Cell using SCAPS-1D Simulation. *Eur. J. Sci. Technol*. 2021;31:121-126. doi:10.31590/ejosat.951602

76. Kramer IJ, Sargent EH. The architecture of colloidal quantum dot solar cells: Materials to devices. *Chem. Rev.* 2014;114(1):863-882. doi:10.1021/cr400299t
77. Ono M, Nishihara T, Ihara T, et al. Impact of surface ligands on the photocurrent enhancement due to multiple exciton generation in close-packed nanocrystal thin films. *Chem. Sci.* 2014;5(7):2696-2701. doi:10.1039/c4sc00436a
78. Gao Y, Aerts M, Sandeep CSS, et al. Photoconductivity of PbSe quantum-dot solids: Dependence on ligand anchor group and length. *ACS Nano.* 2012;6(11):9606-9614. doi:10.1021/nn3029716
79. Mičić OI, Ahrenkiel SP, Nozik AJ. Synthesis of extremely small InP quantum dots and electronic coupling in their disordered solid films. *Appl. Phys. Lett.* 2001;78(25):4022-4024. doi:10.1063/1.1379990
80. Hacıfendioğlu T., Kolay İ., Aydın F., Yıldırım E. and Asil D., “Role of the Ligand Structure in Degree of Organization and Photovoltaic Performance of the PbSe Nanorods”, Under Review
81. <https://imagej.nih.gov/ij/download.html>



## APPENDICES

### A. APP-1

#### UPS spectrum of PbSe NR

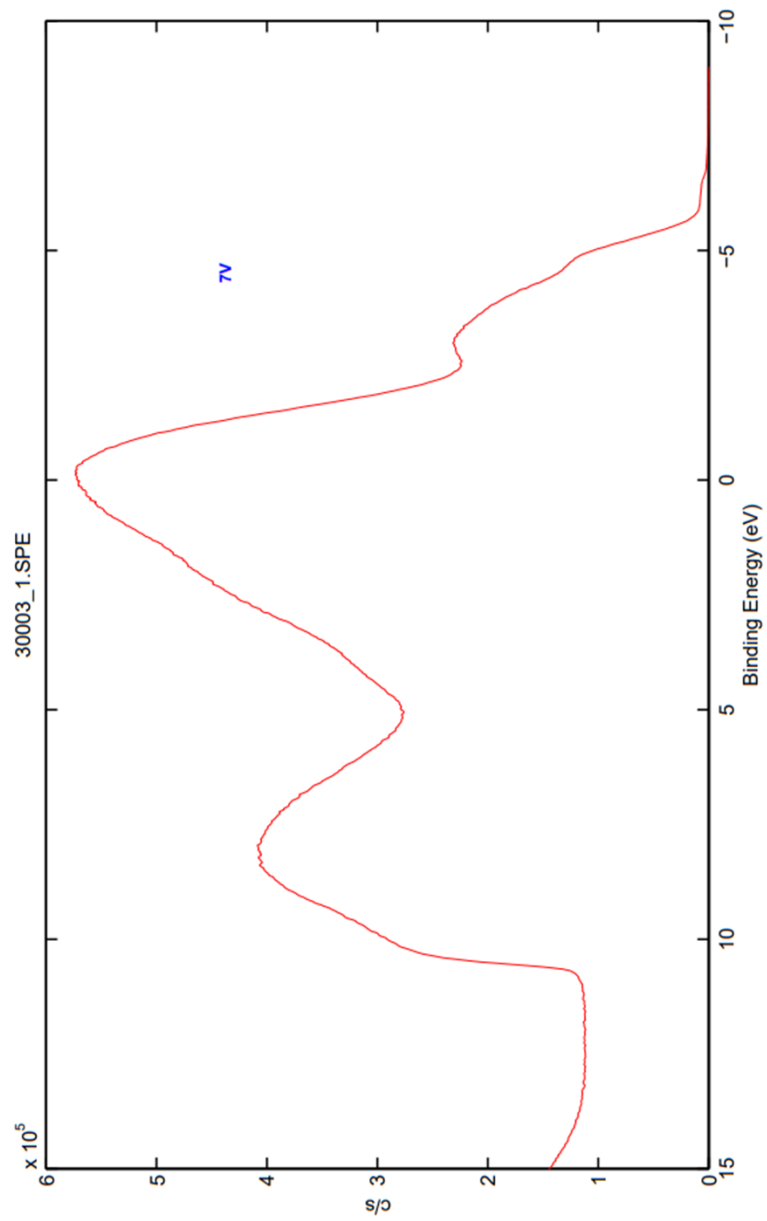


Figure 6.1. UPS spectrum of PbSe NR

## B. APP-2

### UPS spectrum of SynP-PbSe QD

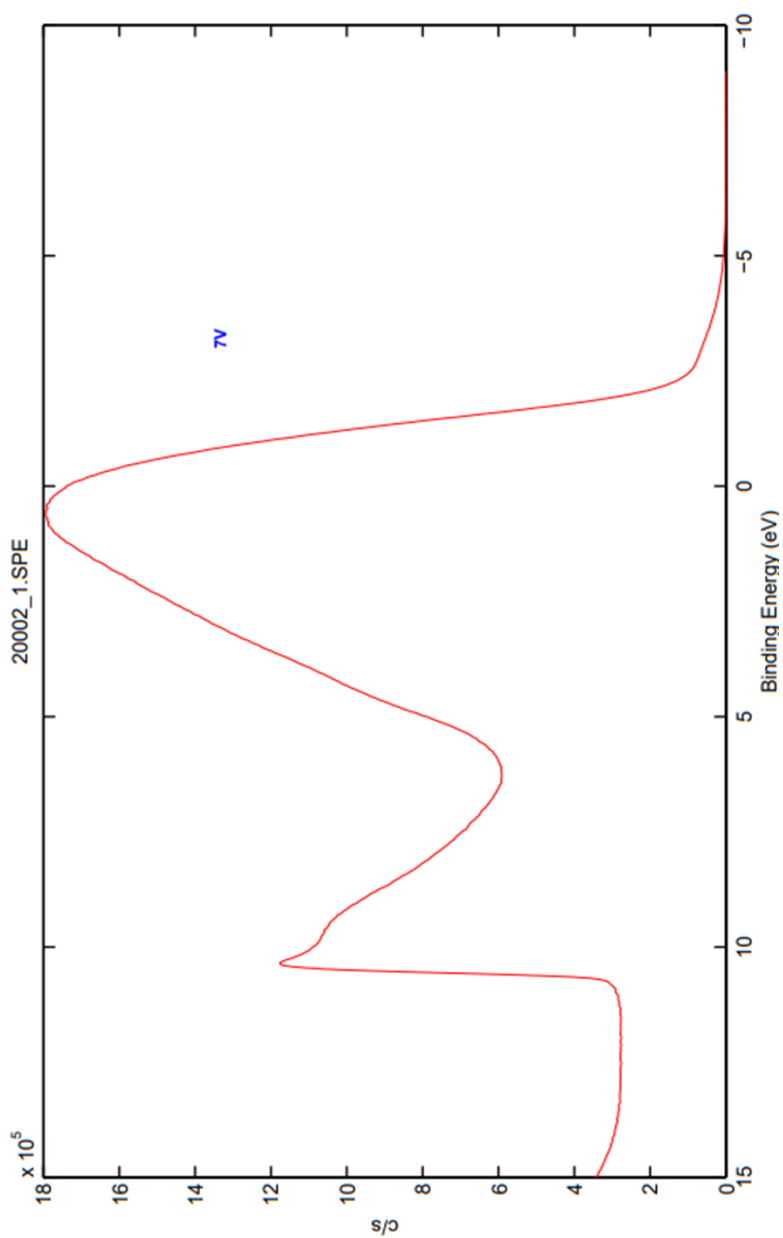


Figure 6.2. UPS spectrum of SynP-PbSe NR

### C. APP-3

#### UPS spectrum of PbSe QD

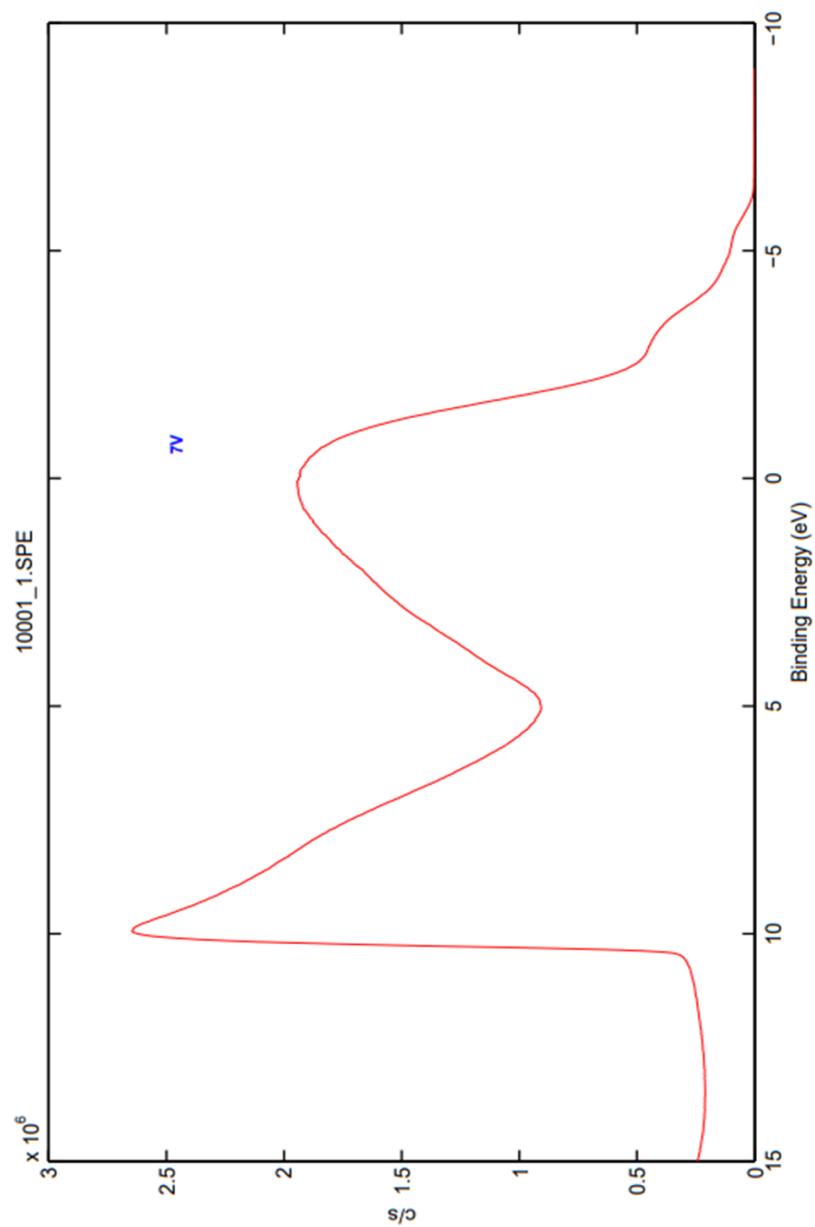


Figure 6.3. UPS spectrum of PbSe QD

## D. APP-4

### UPS spectrum of TIPS-Pentacene

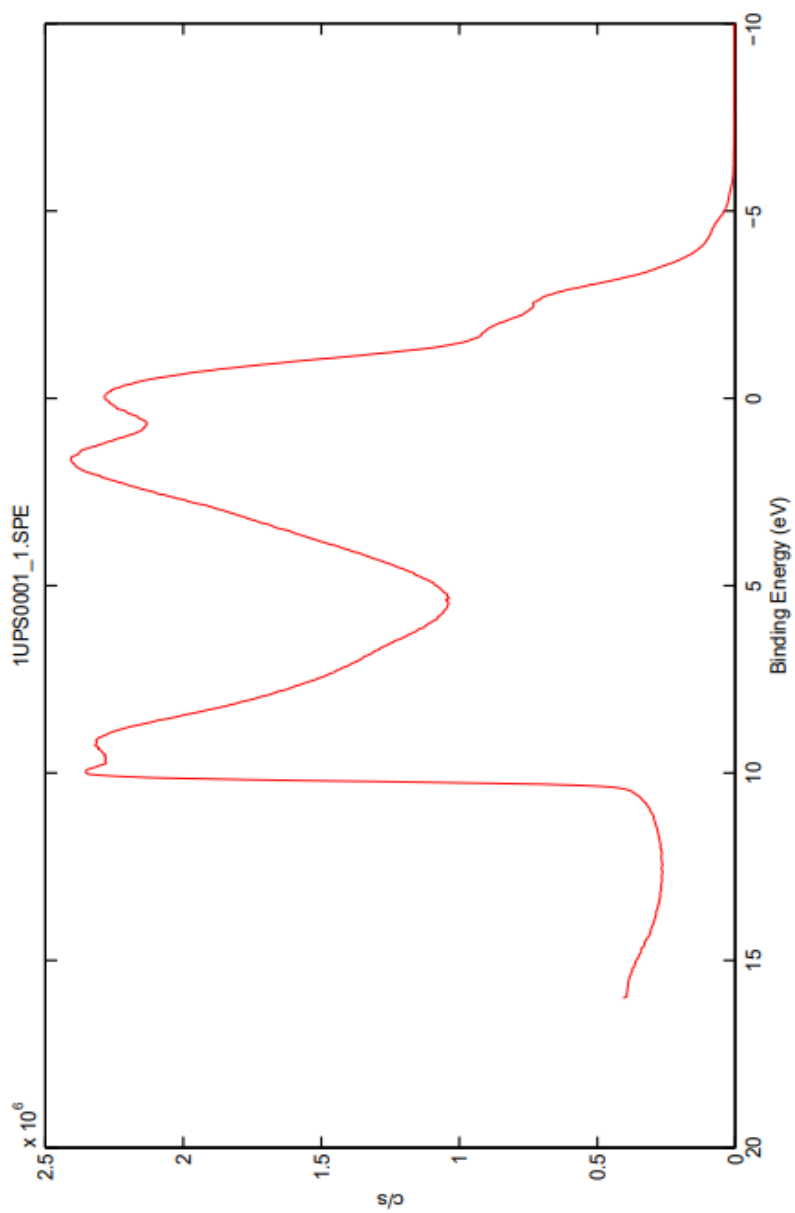


Figure 6.4. UPS spectrum of TIPS-Pentacene